HEALTH AND MEDICINE

Activation of CGRP receptor–mediated signaling promotes tendon-bone healing

Xibang Zhao[1], Guanfu Wu[2], Jing Zhang[2], Ziyi Yu[2], Jiali Wang[1]*

Calcitonin gene-related peptide (CGRP), an osteopromotive neurotransmitter with a short half-life, shows increase while calcitonin receptor-like (CALCRL) level is decreased at the early stage in bone fractures. Therefore, the activation of CALCRL-mediated signaling may be more critical to promote the tendon-bone healing. We found CGRP enhanced osteogenic differentiation of BMSCs through PKA/CREB/JUNB pathway, contributing to improved sonic hedgehog (SHH) expression, which was verified at the tendon-bone interface (TBI) in the mice with *Calcrl* overexpression. The osteoblast-derived SHH and slit guidance ligand 3 were reported to favor nerve regeneration and type H (CD31^{hi}EMCN^{hi}) vessel formation, respectively. Encouragingly, the activation or inactivation of CALCRL-mediated signaling significantly increased or decreased intensity of type H vessel and nerve fiber at the TBI, respectively. Simultaneously, improved gait characteristics and biomechanical performance were observed in the *Calcrl* overexpression group. Together, the gene therapy targeting CGRP receptor may be a therapeutic strategy in sports medicine.

INTRODUCTION

Each year, more than two million anterior cruciate ligament (ACL) injuries occur around the world at an estimated annual cost of 70 billion US dollars (*1*, *2*). Although most of the patients can restore their knee function after ACL reconstruction, the long-term failure rate is still over 10% (*3*). Tendon graft–bone healing quality has been widely considered as one of the most challenging factors influencing clinical outcomes in patients due to the complexity from soft to hard tissue (*4*). Failed reconstruction requires a second revision surgery, leading to economic and physical burden to patients with increased risks suffering osteoarthritis in knee joints (*5*). Enormous evidence revealed that the enhancement of bony ingrowth toward the tendon-bone interface (TBI) may promote the graft healed at the enthesis (*6*–*8*).

Recently, a specific vessel subtype called a type H vessel, which was identified as highly positive for endomucin (EMCN) and CD31, has been reported to favor osteogenic differentiation of the osteoprogenitor cells densely surrounding type H vessels through modulation of angiogenesis-osteogenesis coupling effects (*9*, *10*). Type H blood vessels are mainly distributed in the metaphysis, periosteum, and endosteum (*11*). In ACL reconstruction, the bone tunnel will pass through the metaphysis region with abundant type H vessels, indicating that CD31^{hi}EMCN^{hi} endothelium may be involved in the angiogenesis during the tendon-bone healing.

Our previous work reported calcitonin gene-related peptide (CGRP), a neurotransmitter rich in periosteum and bone marrow, favored the expression of pro-osteogenic mediators during bone fracture healing through activation of the cyclic adenosine 3′,5′-monophosphate (cAMP)/cAMP response element–binding protein (CREB) signaling pathway (*12*). We found the tendon graft wrapped by the CGRP-rich periosteum after magnesium (Mg) pretreatment showed enhanced osteointegration ability (*13*). Although CGRP has been recently tried for direct use in a patellectomy model to test its role in the TBI healing (*14*), the very short half-life (only 5 min in blood) of this neuropeptide would undoubtedly affect its long-term use especially in bone marrow–rich environment (*15*). The level of the pro-osteogenic neuropeptide CGRP is increased at the fracture site in animals (*16*–*19*) and patients (*20*, *21*). However, it was reported that the expression level of CGRP receptor (CALCRL) at the fracture site was low at the early healing stage (day 7 after fracture in mice) while markedly increased at the middle healing stage (day 14 after fracture) (*18*). Therefore, it is necessary to increase the expression levels of CGRP receptor on the cells located at the predrilled tunnel to initiate activation of CGRP-mediated signaling at the early healing stage after surgery. Gene therapy such as delivery of short hairpin RNAs (shRNAs) and DNA plasmids at a tissue level is a potential strategy to modulate CGRP signaling pathway through regulation of CGRP receptor expression. For example, the overexpression of Calcrl was beneficial for osteogenic differentiation of osteoprogenitors, resulting in enhanced bone regeneration at the fracture region (*12*).

As reported in the literatures, the sonic hedgehog (SHH) favors nerve axon regeneration (*22*). SHH was detected in osteoblasts (*23*), indicating the favorable role of osteoblasts in driving outgrowth of sensory axons. On one hand, the neurotransmitters [norepinephrine (NE) or CGRP] secreted by the TH^{+} (tyrosine hydroxylase) sympathetic (*24*) or sensory nerve fibers (*12*) are closely involved in bone modeling and remodeling. On the other hand, osteoclast-derived netrin-1 and osteoblast-secreted SHH have been found to induce nerve axon growth (*25*, *26*), indicating that the communication between skeletal and neural tissues is critical for bone regeneration (*27*). Therefore, the activation of CGRP/CGRP receptor–mediated signaling pathway may drive innervation by promoting SHH production in osteoblasts, which subsequently activate macrophage recruitment (*22*) and proliferation of endogenous neural precursor cells (*26*, *28*). Meanwhile, slit guidance ligand 3 (SLIT3) is highly expressed in osteoblasts, which may simultaneously promote the formation of type H vessels and ultimately positively regulate bone regeneration (*29*). As the overexpression of the CGRP receptor in the osteoprogenitor cells favored their osteogenic differentiation under the stimuli of CGRP, the increased number of osteoblasts may contribute to the enhanced angiogenesis through secretion of more SLIT3 at the

[1]School of Biomedical Engineering, Shenzhen Campus of Sun Yat-Sen University, Shenzhen 518107, Guangdong, P. R. China. [2]State Key Laboratory of Materials-Oriented Chemical Engineering, College of Chemical Engineering, Nanjing Tech University, Nanjing, 211816, P. R. China.
*Corresponding author. Email: wangjli8@mail.sysu.edu.cn

TBI. Collectively, overexpression of CGRP receptor in bone tunnels may modulate innervation and angiogenesis, thereby favoring the graft osteointegration.

Here, to achieve localized drug retention, we propose in this study to inject adenovirus-mediated sh*Calcrl* (adv-sh*Calcrl*)– or *Calcrl* (adv-*Calcrl*)–loaded hydrogel microparticles (HMPs) into bone tunnels in mice that underwent ACL reconstruction. Accordingly, we raised the hypothesis that the graft osteointegration at the bone tunnels would be significantly promoted in the adv-*Calcrl*–treated mice compared to that in the control and adv-sh*Calcrl* groups through modulation of osteogenesis-angiogenesis and osteogenesis-innervation coupling effects by up-regulation of osteoblast-derived SHH and SLIT3 levels. To test the hypothesis, we attempted to (i) further unravel CGRP signaling pathway in osteogenic differentiation of mesenchymal stem cells in vitro and (ii) verify whether the activation of CGRP receptor–mediated signaling affect the tendon graft healing through regulation of angiogenesis and innervation at the TBI.

RESULTS

CGRP promotes the osteogenic differentiation of BMSCs through PKA/CREB/JUNB signaling pathway, favoring higher expression of SHH

As evidenced by Fig. 1A, compared to the normal osteogenic medium, the addition of CGRP significantly increased gene expression levels of *Calcrl* and osteogenic markers, including *Runx2*, *Sp7*, *Ocn*, and *Opn* in mouse bone marrow–derived mesenchymal stem cells (BMSCs). In addition, the formation of the calcium nodules was also

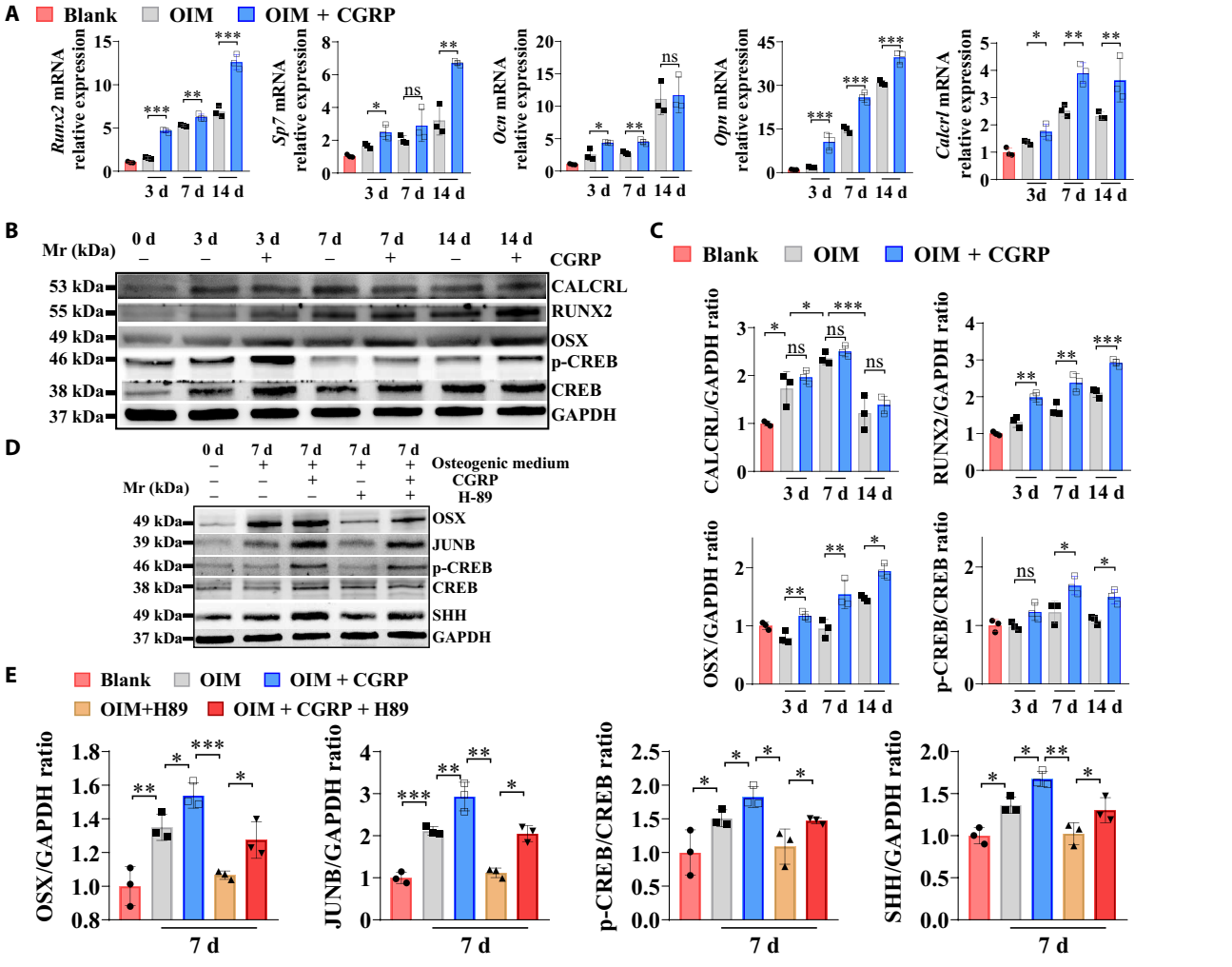

Fig. 1. The effects of CGRP on the osteogenic differentiation capability of mouse BMSCs. (**A**) Real-time polymerase chain reaction (PCR) analysis of *Sp7*, *Runx2*, osteocalcin (*Ocn*), osteopontin (*Opn*), and *Calcrl* mRNA expression in the bone marrow–derived mesenchymal stem cells (BMSCs) after incubation in OIM with or without CGRP. **P* < 0.05, ***P* < 0.01, and ****P* < 0.001; *n* = 3 independent biological replicates. (**B**) Western blot (WB) analysis of protein levels of RUNX2, OSX, p-CREB, CREB, CALCRL, and glyceraldehyde-3-phosphate dehydrogenase (GAPDH) in BMSCs with or without treatment of CGRP. (**C**) Quantification of RUNX2/GAPDH ratio, OSX/GAPDH ratio, and p-CREB/CREB ratio, and CALCRL/GAPDH ratio by WB analysis from (B). ns, not significant, **P* < 0.05, ***P* < 0.01, and ****P* < 0.001; *n* = 3 independent biological replicates. (**D**) WB analysis of protein levels of OSX, JUNB, SHH, p-CREB, CREB, and GAPDH in BMSCs with or without treatment of CGRP or H-89, a selective inhibitor of cAMP-dependent protein kinase (PKA). d, days. (**E**) Quantification of OSX/GAPDH ratio, JUNB/GAPDH, p-CREB/CREB ratio, and SHH/GAPDH ratio by WB analysis from (D). **P* < 0.05, ***P* < 0.01, and ****P* < 0.001; *n* = 3 independent biological replicates. The Blank indicates BMSCs without incubation in osteogenic induction medium (OIM).

significantly increased in both mouse and human BMSCs after CGRP treatment during osteogenic differentiation (fig. S4). Encouragingly, the CGRP stimuli significantly promoted the osteogenic differentiation capability of rat BMSCs and the murine-derived preosteoblast-like cell line, MC3T3-E1 (fig. S5). Consistent with our previous findings performed in periosteum-derived stem cells (*12*), CGRP treatment also activates cAMP-dependent protein kinase (PKA)/CREB signaling pathway during osteogenic differentiation of BMSCs, contributing to higher levels of RUNX2 and Osterix (OSX) (Fig. 1, B and C). The phosphorylation of CREB favored the expression of JUNB, a pro-osteogenic transcription factor, while inhibiting PKA/CREB signaling by H-89, a specific inhibitor to PKA, suppressed the levels of JUNB (Fig. 1, D and E). Of note, the expression level of SHH was significantly increased when the BMSCs were induced toward osteogenic differentiation. The addition of CGRP in the osteogenic medium significantly increased the expression level of SHH in the BMSC-derived osteoblasts. Meanwhile, the addition of H-89 significantly down-regulated the expression level of SHH in the BMSC-derived osteoblasts with and without CGRP stimuli. The consistent results were also observed in human BMSCs during the course of osteogenic differentiation with or without addition of CGRP and H-89 (fig. S6).

The HMPs exhibiting excellent rheological performance and biocompatibility favor structural stability of adenoviral vector for extended release

To prepare HMPs, uniform microdroplets were first prepared by microfluidic emulsion technique. As is shown in Fig. 2A, aqueous dispersions containing 1% (w/v) thiolated hyaluronic acid (SH-HA), 3.33% (w/v) hyperbranched poly(ethylene glycol) diacrylate macromer (HB-PEGDA), and adenovirus (3.52×10^9 IFU/ml) were intersected by the fluorinert FC-40 oil containing 2 wt % Pico-Surf in a microfluidic droplet maker to generate uniform microdroplets (Fig. 2B). Then, in analogy to a flask in a chemistry lab, each microdroplet here acts as a micro-compartment where HMP is produced by a Michael addition reaction between SH-HA and HB-PEGDA (*30*). As shown in Fig. 2C, HMPs with a diameter of 150 μm and a coefficient of variation of less than 3% were lastly obtained. HMPs of this size were used for subsequent experiments unless otherwise stated. Typical scanning electron microscopy images of HMPs further confirmed that the HMPs were relatively uniform in size and that their surfaces were wrinkled because of shrinkage caused by the freeze-drying process (Fig. 2D).

The resulting HMPs were then concentrated by centrifugation at 10^4 rpm for 10 min before injection. In a continuous flow experiment

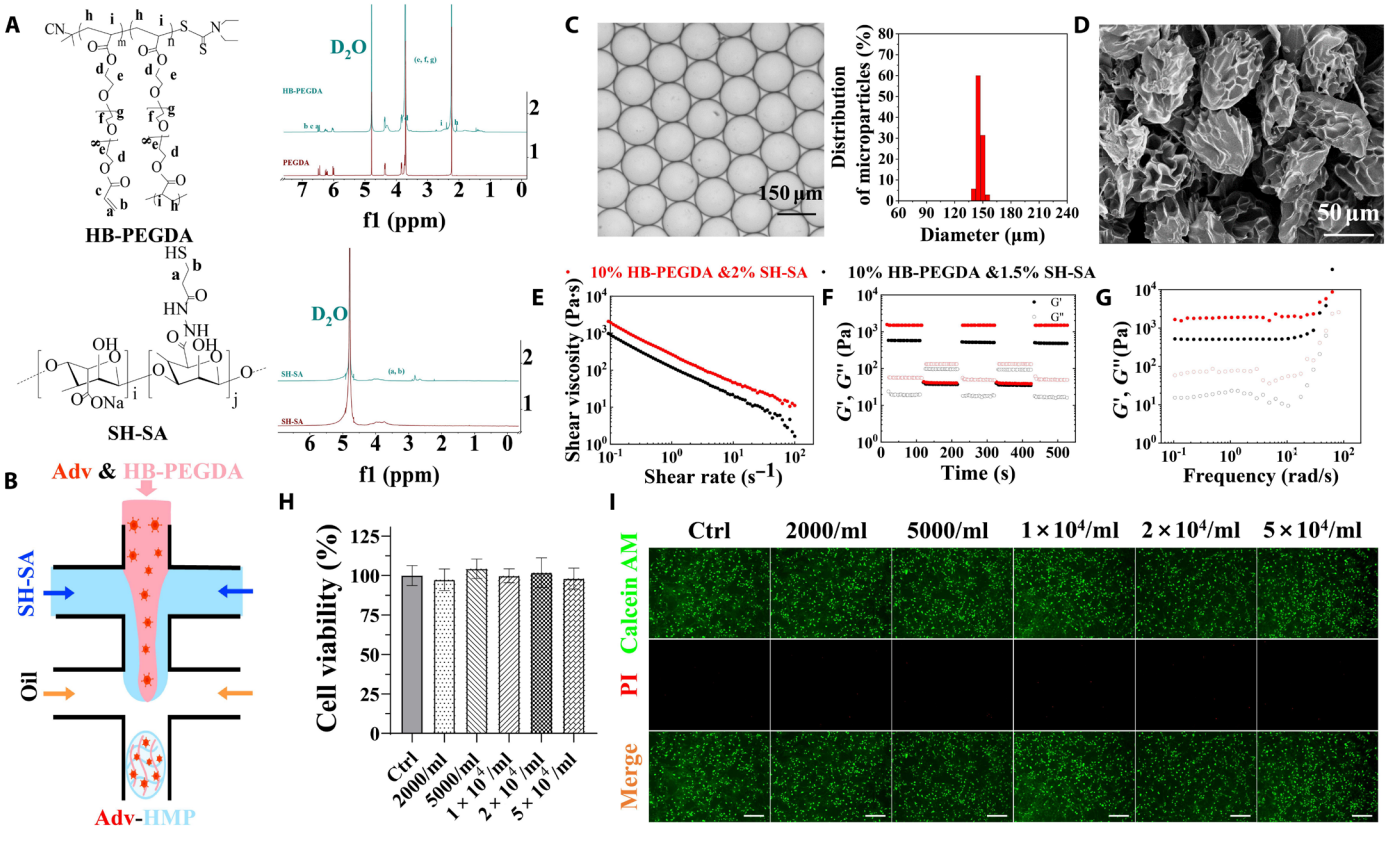

Fig. 2. Synthesis and characterization of HMPs. (**A**) Proton nuclear magnetic resonance (^{1}H NMR) spectra of HB-PEGDA and SH-SA. (**B**) Schematic diagram of the preparation of HMPs in a poly(dimethylsiloxane)-based microfluidic droplet generator device. (**C**) Micrograph and diameter distribution of the resulting microdroplet templates. (**D**) Representative scanning electron microscopy images of the as-obtained HMPs. (**E**) Viscosity as a function of shear rate for the HMP clusters. (**F**) Strain-cycle experiment for the HMP clusters, whereby materials are cycled between 0.1 and 1000% stains. (**G**) The storage (G') and (G'') modulus were measured under a constant strain of 1% and angular frequency ranging from 0.1 to 100 rad/s at 25°C. (**H**) Cell viability of BMSCs exposed to gradient concentration of HMPs. $n = 4$. (**I**) Live/Dead staining of BMSCs incubated with gradient concentrations of HMPs visualized by a calcein AM/propidium iodide (PI) double-staining assay.

(Fig. 2E), the instantaneous viscosity modulus of the concentrated HMPs was measured under a controlled frequency of 1 Hz and a wide range of shear rates from 0.01 to 100 s^{-1}. It reveals that concentrated HMPs present shear-thinning properties. Next, an oscillatory strain alternation between 1000 and 0.1% was applied to these HMP samples at the same frequency (1 Hz). As shown in Fig. 2F, for a high magnitude strain (1000%), the sample exhibits a sol state, as $G'' > G'$. Moreover, when the strain is switched to a low magnitude strain (0.1%), the sol exhibits quick recovery to gel state, indicating self-healing behavior. The characteristics indicate that the concentrated HMPs become viscous and easy to flow under the action of external shear force, which is beneficial for subsequent injectable treatments. When the external force is removed, the HMPs immediately restore the elasticity, realizing local drug retention. In addition, frequency sweeps showed that concentrated HMPs have a G' of 500 Pa, and increasing the concentration of SH-HA from 1 to 1.33% effectively increased the elastic modulus of the material to several thousand pascals, all else being equal (Fig. 2G). The controllable mechanical properties and degradability of the constituent materials make HMPs ideal carriers for biomedical applications. Then, the biocompatibility and cytotoxicity of HMPs were determined with cell counting kit-8 (CCK-8) assay and calcein AM/propidium iodide staining, and HMPs exhibit a good biocompatibility and low cytotoxicity as potential drug delivery systems (Fig. 2, H and I).

Then, the structural stability of adenovirus alone and adenovirus loaded in HMPs was tested and compared to assess which one was more suitable for gene transfection. Of note, the quantitative polymerase chain reaction (qPCR) testing results showed that more than 90% of naked adenoviral vector was degraded after immersion in phosphate-buffered saline (PBS) for 1 day, while the encapsulation of adenovirus particles effectively reduced the degradation of adenoviral vector, showing approximate 54, 76, 95, 95, and 97% loss after 1, 3, 5, 7, and 9 days, respectively (Fig. 3A). Consistently, the agarose gel electrophoresis analysis revealed that most of naked adenoviral vector was degraded rapidly in PBS. Meanwhile, the product band assigned for the adenoviral vector, which was encapsulated by HMPs, was still clearly visualized even after immersion in PBS for 9 days (Fig. 3B). The improved structural stability of adenoviral vectors in HMPs profoundly improved the gene transfection efficiency. After immersion in PBS for 7 days, the adenoviral vectors, containing a green fluorescent protein (GFP), loaded in the HMPs were collected to transfect BMSCs. The adenoviral vectors alone (without HMPs loading), which were directly kept in PBS for 7 days, were also collected for gene transfection. As shown in Fig. 3C, the GFP expression level in BMSCs indicates the transfection efficiency, suggesting that the HMPs favored the structural stability of the adenoviral vectors for higher efficiency of transfection. Accordingly, the sh*Calcrl* or *Calcrl* gene transfection via adenovirus-mediated delivery successfully reduced or increased gene and protein expression levels of CALCRL in the BMSCs after 3 days after transfection (Fig. 3D), contributing to up- or down-regulation of osteogenic markers of BMSCs during osteogenic differentiation with or without CGRP treatment after 7 days (Fig. 3E).

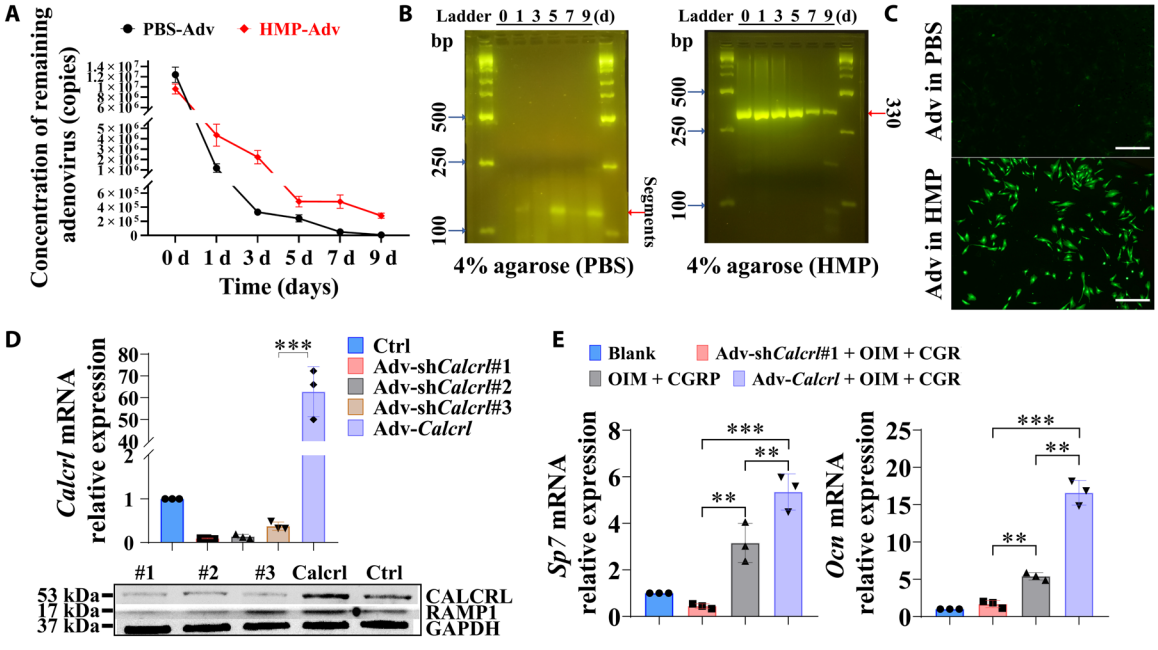

Fig. 3. Transfection efficiency of adenoviral transfer through the HMP delivery system. (**A**) Concentration of remaining adenovirus in HMPs or PBS. $n = 3$ independent experiments. (**B**) Agarose gel electrophoresis of extracted DNA in the remaining adenovirus in HMPs or PBS. (**C**) The adenoviral vectors, expressing a green fluorescent protein (GFP), exhibited enhanced gene transfection efficiency in BMSCs for the adenovirus loaded HMPs compared to the adenovirus alone after immersion in PBS for 7 days. (**D**) Gene and protein expression levels of *Calcrl* in the BMSCs with or without incubation of adv-sh*Calcrl* or adv-*Calcrl* after 3 days. ***$P < 0.001$; $n = 3$ independent biological replicates. (**E**) Gene expression levels of *Sp7* and *Ocn* of BMSCs with or without incubation of adv-sh*Calcrl* or adv-*Calcrl* after osteogenic differentiation in the osteogenic medium with or without addition of CGRP after 7 days. **$P < 0.01$ and ***$P < 0.001$; $n = 3$ independent biological replicates. The Blank indicates BMSCs without incubation in OIM.

The activation of CGRP receptor–mediated signaling enhances osseous ingrowth toward the TBI and promotes intra-tunnel bone formation

Consistently, the local injection of HMPs loading adv-sh*Calcrl* or adv-*Calcrl* into bone tunnels affected tendon graft osteointegration and healing quality according to both hematoxylin and eosin (H&E) and Safranin O/Fast Green staining results (Fig. 4A). Apparently, compared to the injection of HMPs alone, the administration of adv-*Calcrl* encapsulated in HMPs significantly promoted bony ingrowth toward the TBI and accelerated healing process. Although the adv-sh*Calcrl* treatment impaired the tendon-bone healing in terms of assessment outcomes on histological healing scores and tendon-bone contact ratio, there were no significant differences between the adv-*shCalcrl* group and the control group (Fig. 4B). To investigate whether the local injection of adenoviral particles loaded in HMPs successfully transfected the target tissue in vivo, we performed immunostaining of CALCRL and found that the expression of CALCRL was significantly increased in the adv-*Calcrl* group but significantly decreased in the adv-sh*Calcrl* group at 4 and 6 weeks after surgery (Fig. 5). The changes of CALCRL expression levels may lead to activation or inactivation of CGRP receptor–mediated signaling pathway, which was verified by the immunostaining results of JUNB (fig. S7). To further study the effects of CGRP receptor on levels of osteogenic markers, immunostaining of RUNX2 was also performed. Compared to the HMPs alone group, a significantly increased fluorescence intensity of double-positive region for RUNX2 and CALCRL at the TBI was observed in the adv-*Calcrl* group (4.24 ± 0.35 versus 1.12 ± 0.31 at 4 weeks, $P < 0.001$; 4.19 ± 1.01 versus 0.96 ± 0.29 at 6 weeks, $P < 0.01$). Meanwhile, the adv-sh*Calcrl* treatment significantly decreased the fluorescence intensity of double-positive region of RUNX2 and CALCRL relative to the control group (0.13 ± 0.01 versus 1.12 ± 0.31 at 4 weeks, $P < 0.05$; 0.13 ± 0.03 versus 0.96 ± 0.29 at 6 weeks, $P < 0.05$) (Fig. 5).

Therefore, HMPs, as the delivery system of adenoviral particles, effectively protected the degradation of the shuttle plasmid and significantly improved the osseous ingrowth at the TBI through transferring *Calcrl* genes into cells located in bone tunnels. Although bone tunnel expansion after ACL reconstruction is a well-accepted frequent phenomenon, a marked increase in bone tunnel size may reduce the fixation stability of the graft, thereby impairing the graft healing and ultimately causing knee laxity and complicate revision (*31*). To examine whether the activation of CGRP receptor–medicated signaling affects intra-tunnel bone mass, the radiographic measurement was performed by micro–computed tomography (CT). As shown in Fig. 6, compared to the control group and adv-sh*Calcrl* group, the overexpression of *Calcrl* significantly reduced bone tunnel enlargement and increased intra-tunnel bone mass in terms of bone tunnel diameter, relative bone volume ratio (BV/TV), bone mineral density (BMD), trabecular bone number (Tb. N), trabecular bone separation (Tb. Sp), and trabecular bone thickness (Tb. Th), respectively (Fig. 6C). Collectively, all the data supported that the local delivery of adv-*Calcrl* encapsulated in HMPs efficiently promoted the graft osteointegration into bone tunnels and also significantly modified intra-tunnel bone mass.

The activation of CGRP receptor–mediated signaling favors innervation and type H vessel formation at the TBI

Sensory innervation is part of the neural network of the bone tissue, contributing to release of osteogenic neurotransmitters at the nerve endings, such as CGRP, thereby favoring bone regeneration in the region rich of neuropeptides (*25*, *27*). Compared to the control group, the adv-*Calcrl* group significantly increased $RUNX2^{+}SHH^{+}$ bone tissue around the tendon graft at 1 and 2 weeks after surgery (1.37 ± 0.16 versus 1.00 ± 0.03 at 1 week, $P < 0.01$; 1.84 ± 0.05 versus 0.98 ± 0.08 at 2 weeks, $P < 0.0001$), while the adv-sh*Calcrl* group displayed a significantly decreased $RUNX2^{+}SHH^{+}$ bone (0.66 ± 0.05 versus 1.00 ± 0.03 at 1 week, $P < 0.05$; 0.27 ± 0.08 versus 0.98 ± 0.08 at 2 weeks, $P < 0.0001$) (Fig. 7, A and C). Even at 4 and 6 weeks after surgery, as compared to the control group, the adv-*Calcrl* group still significantly increased SHH expression level, while the adv-sh*Calcrl*

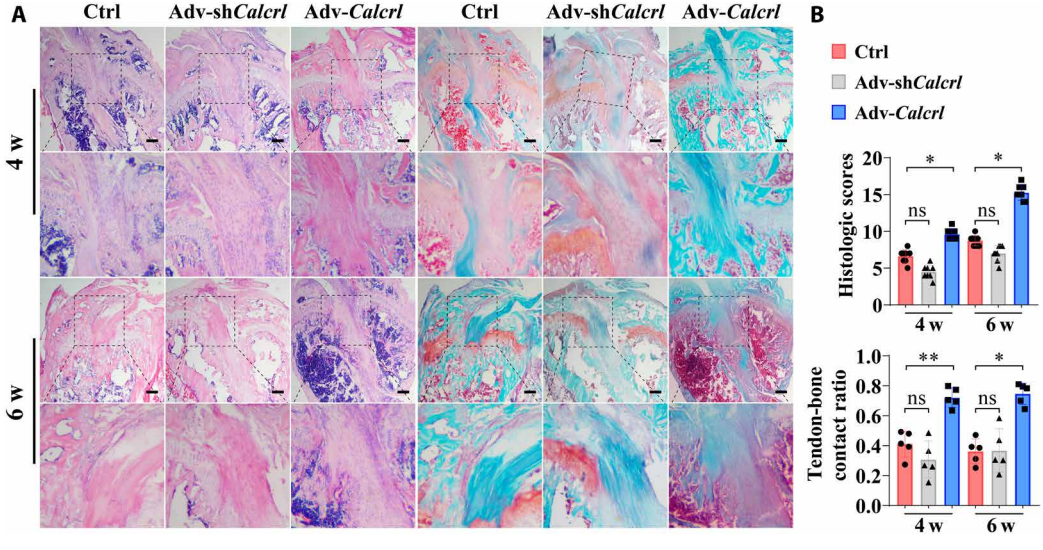

Fig. 4. Histological staining examination for the TBI. (**A**) Representative hematoxylin and eosin (H&E) and Safranin-O/Fast Green staining images showing tendon-bone healing at 4 and 6 weeks (w) after surgery. The black dashed squares indicated the magnified region at the tendon-bone interzone. Scale bars, 200 μm. (**B**) Semiquantitative analysis of the tendon-bone healing quality. ns, not significant, $^{*}P < 0.05$, and $^{**}P < 0.01$; $n = 5$.

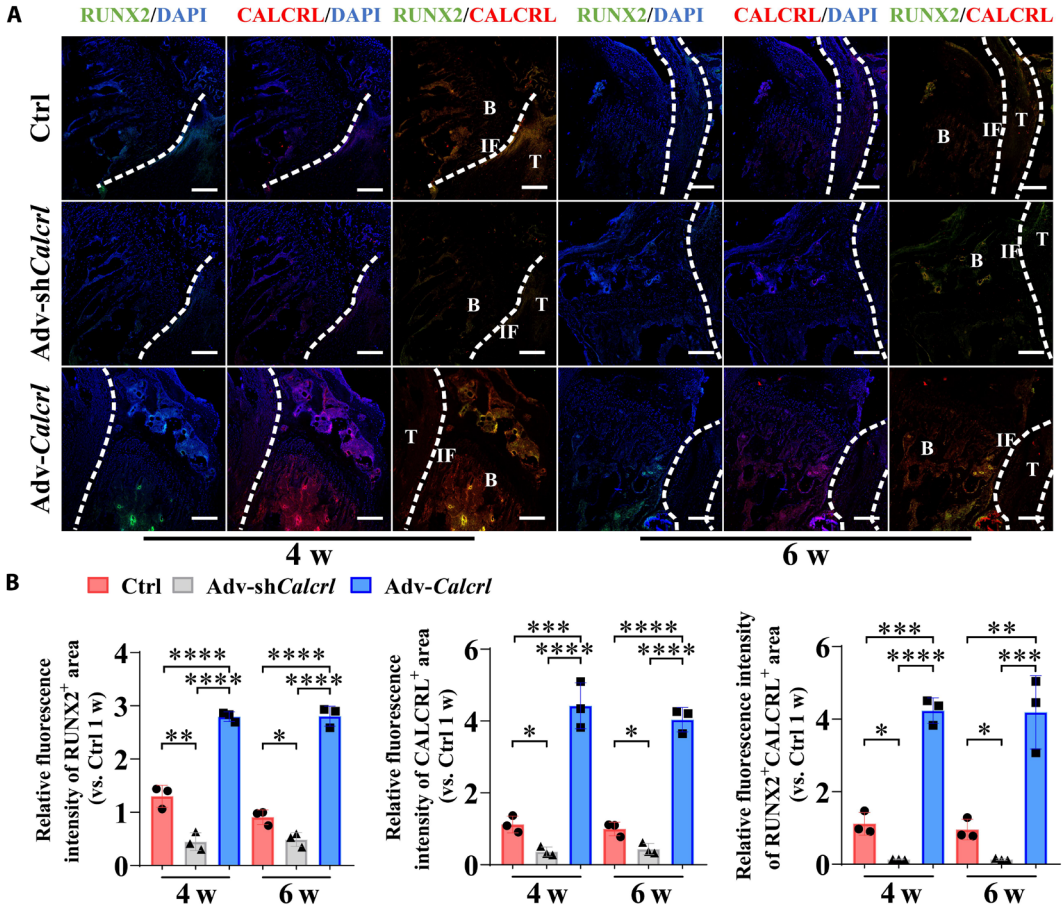

Fig. 5. CGRP receptor–mediated signaling modulates expression levels of RUNX2 and CALCRL at the TBI in mice. (**A**) Representative immunofluorescence staining of RUNX2 and CALCRL at the TBI in mice with various treatments at 4 and 6 weeks after surgery. DAPI, 4′,6-diamidino-2-phenylindole. (**B**) Quantitative analysis of the relative fluorescence intensities of $RUNX2^+$, $CALCRL^+$, and $RUNX2^+CALCRL^+$ area at the TBI in mice with various treatments at 4 and 6 weeks after surgery. $^*P < 0.05$, $^{**}P < 0.01$, $^{***}P < 0.001$, and $^{****}P < 0.0001$; $n = 3$. Dashed lines, tendon graft boundary; B, bone; T, tendon; IF, interface. Scale bars, 200 μm.

group significantly decreased SHH expression level at the TBI (fig. S8). Simultaneously, the local injection of adv-*Calcrl*–loaded HMPs significantly increased the relative density of $CGRP^+NF200^+$ nerve fibers (1.49 ± 0.10 versus 1.00 ± 0.13 at 1 week, $P < 0.01$; 1.99 ± 0.25 versus 1.11 ± 0.09 at 2 weeks, $P < 0.01$), while the adv-sh*Calcrl* administration significantly decreased $CGRP^+NF200^+$ nerve fibers (0.27 ± 0.10 versus 1.00 ± 0.13 at 1 week, $P < 0.001$; 0.25 ± 0.06 versus 1.11 ± 0.09 at 2 weeks, $P < 0.01$) at the TBI (Fig. 7, B and C), indicating that the activation of CGRP receptor–mediated signaling was positively correlated with innervation by $CGRP^+NF200^+$ sensory fibers. Encouragingly, when compared to the control group, the adv-*Calcrl* group still showed significantly increased fluorescence intensity of $CGRP^+NF200^+$ area, while the adv-sh*Calcrl* group exhibited significantly decreased fluorescence intensity of $CGRP^+NF200^+$ area at the TBI at 4 and 6 weeks after surgery (fig. S8).

The enhancement of osteogenic differentiation of BMSCs was accompanied with the up-regulation of SLIT3 (*29*), a proangiogenic factor influencing the number of type H vascular endothelial cells. We then questioned whether the modulation of CGRP receptor–mediated signaling affected the type H vessel formation at the TBI. As shown in Fig. 8 (A and C), compared to the control group, the adv-*Calcrl* group significantly increased the osteoblast-derived SLIT3 expression level ($RUNX2^+SLIT3^+$) (1.86 ± 0.10 versus 1.00 ± 0.04 at 1 week, $P < 0.0001$; 2.11 ± 0.23 versus 1.03 ± 0.04 at 2 weeks, $P < 0.001$), while the administration of adv-sh*Calcrl* significantly reduced the osteoblast-derived SLIT3 expression level (0.31 ± 0.08 versus 1.00 ± 0.04 at 1 week, $P < 0.0001$; 0.25 ± 0.11 versus 1.03 ± 0.04 at 2 weeks, $P < 0.01$) at the TBI at 1 and 2 weeks after surgery. Simultaneously, as compared to the control group, the adv-*Calcrl* group showed a significant increase in the formation of $CD31^{hi}EMCN^{hi}$ endothelium, while the adv-sh*Calcrl* group significantly reduced levels of $CD31^{hi}EMCN^{hi}$ endothelium at 1, 2, 4, and 6 weeks after surgery (Fig. 8, B and C).

Our in vitro data showed that the gene and protein expression levels of CGRP receptor (CALCRL) were relative lower in BMSCs and then significantly increased after 3 days in the course of osteogenic differentiation. As evidenced by the in vivo data, the fluorescence intensity of *CALCRL* was significantly decreased in the trabecular bone of mice at 1 and 2 weeks after surgery relative to that in mice without surgery (fig. S9), which may be ascribed to the increased number of recruited BMSCs at the injured site. The fluorescence intensity of CGRP was significantly increased around the predrilled bone tunnel

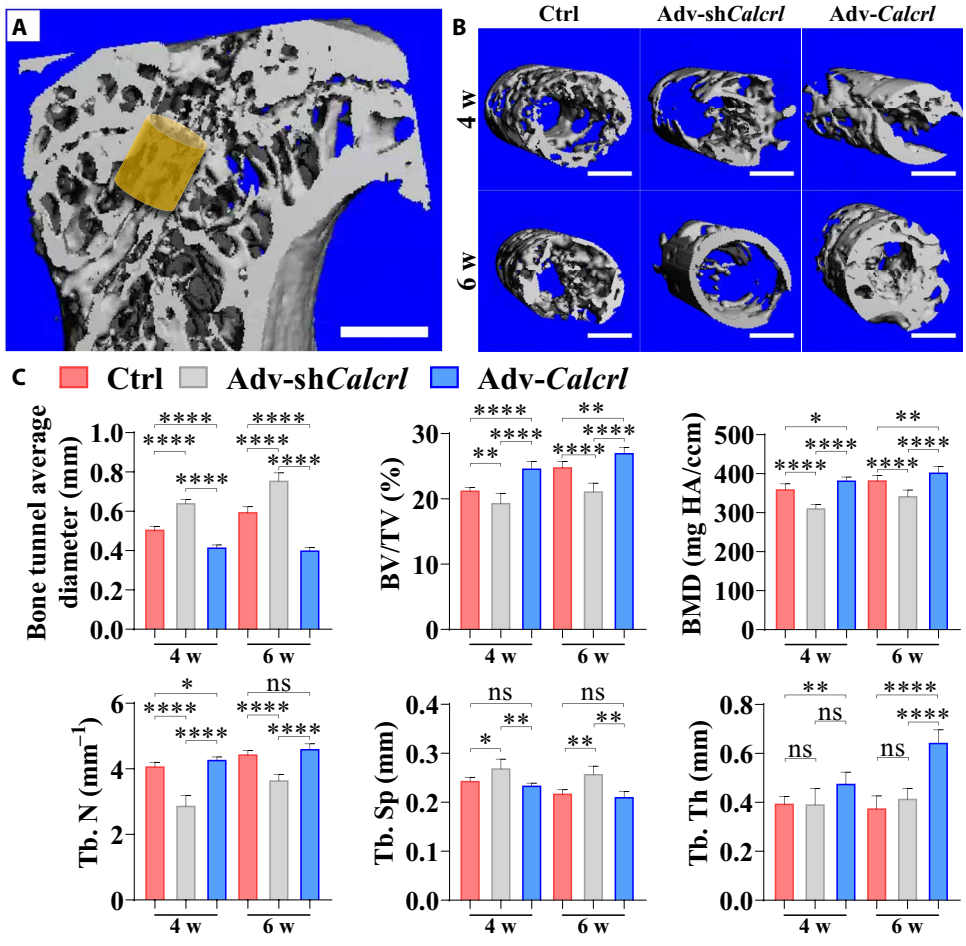

Fig. 6. Micro-CT analysis results for peri-tunnel bone in tibia. (**A**) Region of interest (ROI) indicated by the yellow cylinder of 0.8 mm in diameter and 0.54 mm in height located around the metaphysis. Scale bar, 1 mm. (**B**) Representative three-dimensional reconstructed images showing intra-tunnel bone tissue in ROI in different groups at the indicated time points. (**C**) Quantitative analysis of bone tunnel diameters, relative bone volume (BV/TV), bone mineral density (BMD), trabecular number (Tb. N), trabecular separation (Tb. Sp), and trabecular thickness (Tb. Th) at different groups at the indicated time points. *$P < 0.05$, **$P < 0.01$ and ****$P < 0.0001$; $n = 4$ to 5.

in mice from the presurgery to the after surgery (fig. S9). Therefore, the activation of CGRP receptor–mediated signaling was an efficient strategy to regulate both nerve fiber and type H vessel formation at the at the TBI, which may in turn favor new bone formation through coupling the densely surrounded osteoprogenitors around type H vessels (*10*) and releasing the pro-osteogenic neurotransmitters, e.g., CGRP (*12*), respectively.

The activation of CGRP receptor–mediated signaling improves knee function of mice after ACL reconstruction

Successful ACL reconstruction with appropriate treatment can usually restore stability and function of knees, so gait analysis and biomechanical testing were further performed to verify whether the activation of CGRP receptor–mediated signaling successfully modify knee function and stability. The mice underwent ACL reconstruction displayed significant decrease in stride length and print area while significant increase in paw overlap distance relative to mice in both healthy and sham groups (Fig. 9, A to D). Then, the effects of adenoviral treatment on gait characteristics and kinetic parameters of mice were observed and recorded. Of note, in terms of stride length, as compared to the control group, the mice in the adv-*Calcrl* group revealed a significant increase at 2, 4, and 6 weeks after surgery (Fig. 9B). For print area, the mice showed a significant increase in the adv-*Calcrl* group compared to that in the control group at 4 weeks after surgery (Fig. 9C). In addition, the hind paws of mice exhibited a significant decrease of paw overlap distance in the adv-*Calcrl* group compared to the control group at 4 and 6 weeks after surgery (Fig. 9D). Different from adv-*Calcrl* treatment, the adv-sh*Calcrl* injection showed opposite effects on these kinetic parameters. Therefore, these data indicated that the activation of CGRP receptor–medicated signaling significantly modified gait behavior in mice with ACL reconstruction.

The improved knee function may be correlated with enhanced tendon-bone bonding strength. To test this hypothesis, biomechanical testing was conducted to compare failure mode, maximal failure load, stiffness, and laxity displacement in the femur–tendon graft–tibia complex (FTGTC) from mice with various treatment (Fig. 10A). After reconstruction, the ligament failure mode covered midsubstance, tibial insertion tunnel, and femoral insertion tunnel (Fig. 10B). Compared to the control group, the adv-*Calcrl* group

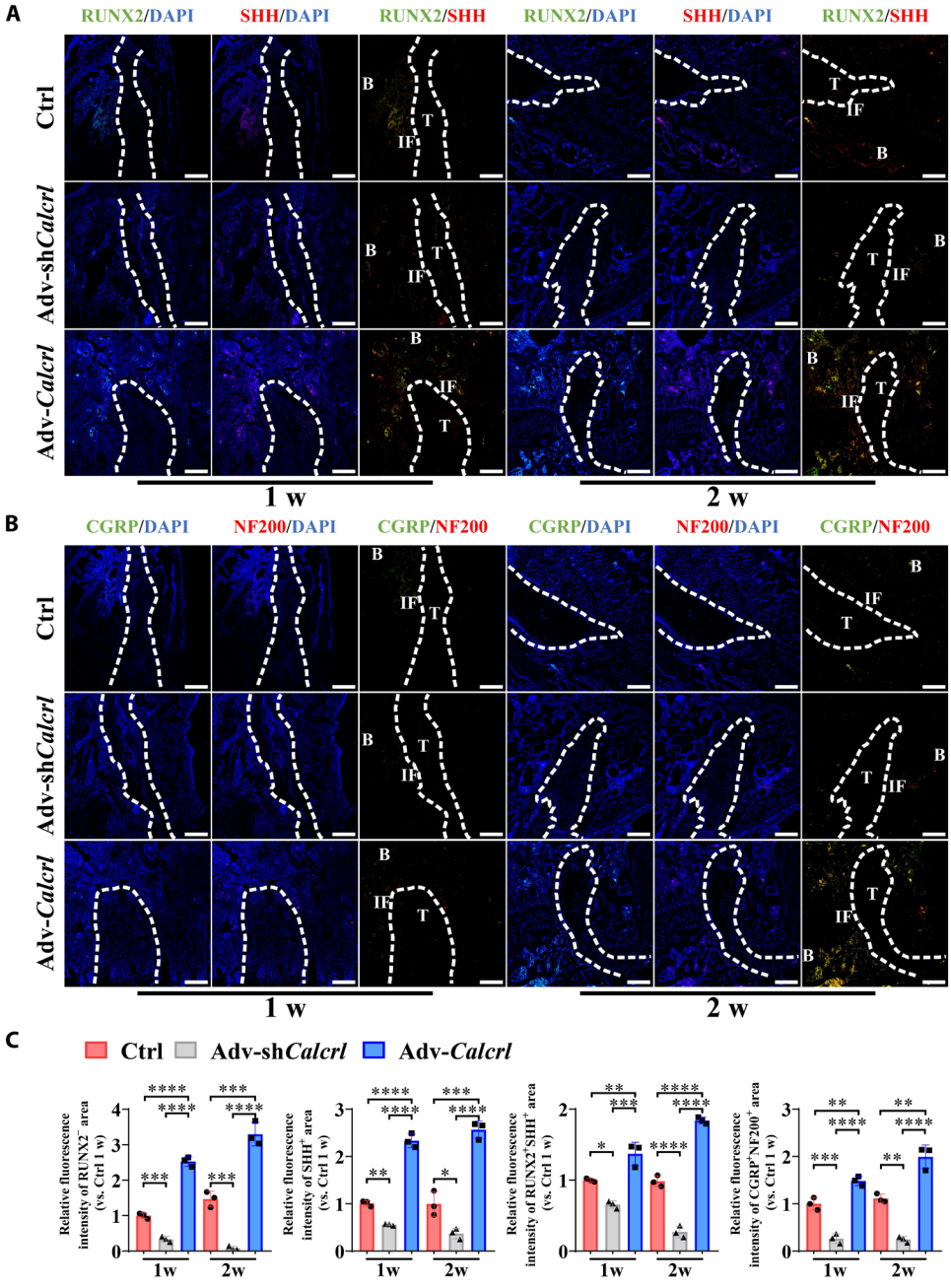

Fig. 7. CGRP receptor–mediated signaling modulates expression levels of RUNX2, SHH, CGRP, and NF200 at the TBI in mice. (**A**) Representative immunofluorescence staining of RUNX2 and SHH at the TBI in mice with various treatments at 1 and 2 weeks after surgery. (**B**) Representative immunofluorescence staining of CGRP and NF200 at the TBI in mice with various treatments at 1 and 2 weeks after surgery. (**C**) Quantitative analysis of the relative fluorescence intensities of $RUNX2^+$, SHH^+, $RUNX2^+SHH^+$, and $CGRP^+NF200^+$ area at the TBI in mice with various treatments at 1 and 2 weeks after surgery. $^*P < 0.05$, $^{**}P < 0.01$, $^{***}P < 0.001$, and $^{****}P < 0.0001$; $n = 3$. Dashed lines, tendon graft boundary; B, bone; T, tendon; IF, interface. Scale bars, 200 μm.

showed a significant increase in the maximum load to failure at 6 weeks and a significant reduction in knee laxity displacement at 4 weeks after surgery (Fig. 10C). On the contrary, the adv-sh*Calcrl* injection significantly decreased the maximum load to failure and also substantially reduced graft stiffness relative to the control group (Fig. 10C). These data revealed that the activation of CGRP receptor–mediated signaling was beneficial for higher bonding strength and knee stability (less laxity displacement) in reconstructed subjects.

DISCUSSION

The purpose of this study was to develop an adenovirus-mediated gene therapy targeting bone tunnels for enhancement of tendon-bone

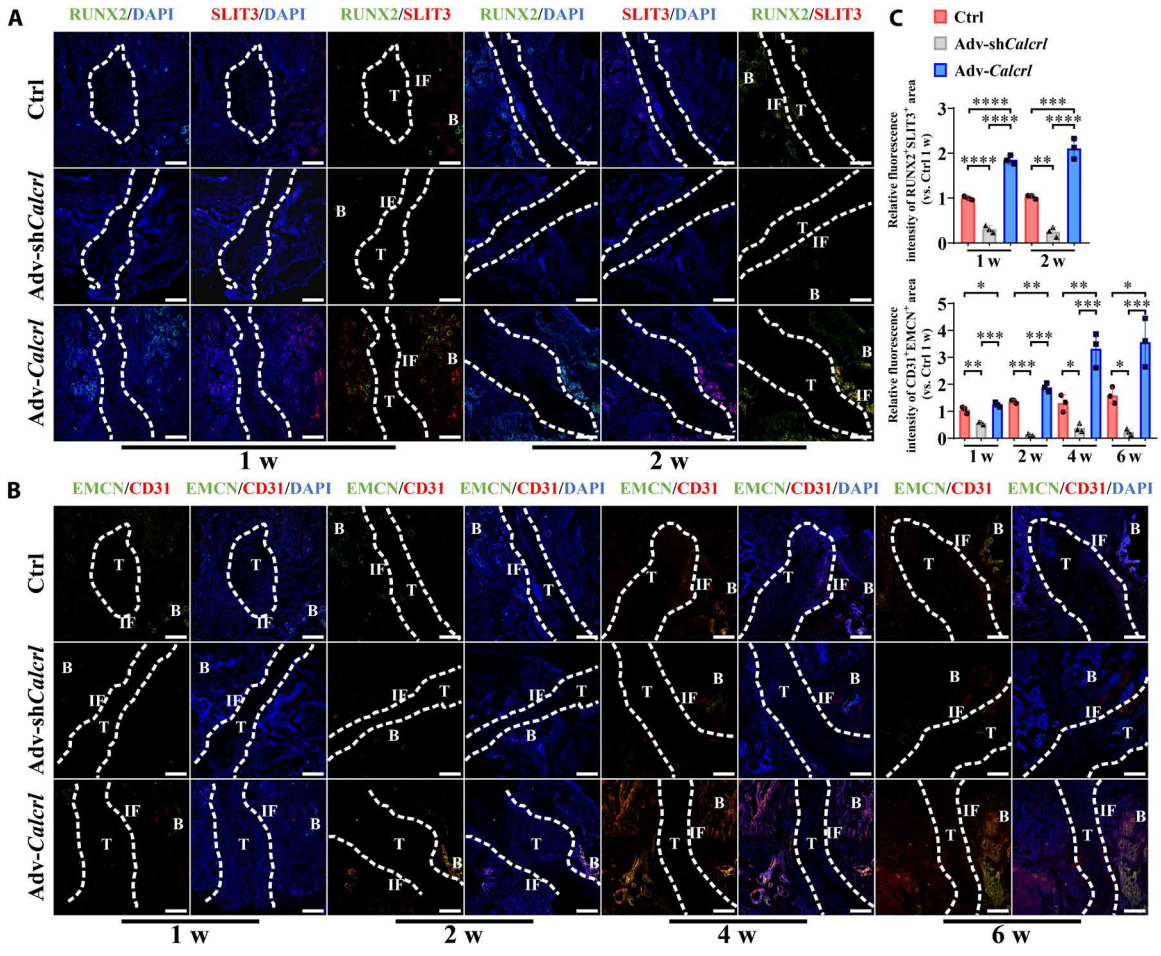

Fig. 8. CGRP receptor–mediated signaling modulates expression levels of RUNX2, SLIT3, EMCN, and CD31 at the TBI in mice. (**A**) Representative immunofluorescence staining of RUNX2 and SLIT3 at the TBI in mice with various treatments at 1 and 2 weeks after surgery. (**B**) Representative immunofluorescence staining of EMCN and CD31 at the TBI in mice with various treatments at 1, 2, 4, and 6 weeks after surgery. (**C**) Quantitative analysis of the relative fluorescence intensities of $RUNX2^{+}SLIT3^{+}$ and $CD31^{+}EMCN^{+}$ area at the TBI in mice with various treatments at the indicated time points after surgery. $^{*}P < 0.05$, $^{**}P < 0.01$, $^{***}P < 0.001$, and $^{****}P < 0.0001$; $n = 3$. Dashed lines, tendon graft boundary; B, bone; T, tendon; IF, interface. Scale bars, 200 μm.

healing. We verified that the activation of CGRP/CGRP receptor–mediated signaling promoted osteogenic differentiation of BMSCs via regulation of PKA/CREB/JUNB axis. The osteoprogenitor cells, as the predominant cell type transfected by the adenovirus expressing *Calcrl* at the TBI in mice, also increased significantly in the adv-*Calcrl* group relative to that in the control group. The increased number of osteoprogenitors significantly favored the osteoblast-derived SHH and SLIT3 expression at the TBI in the adv-*Calcrl* group relative to that in the control group, which may thereby contribute to significantly enhanced regeneration of nerve fiber and type H vessel formation, respectively.

CGRP, a short neuropeptide with two major forms (α and β) associated with C and Aδ sensory fibers, is mainly distributed throughout the central and peripheral nervous systems (*32*). Recently, mounting evidence suggests that α-CGRP initiated signaling highly influences bone regeneration (*18*). Our previous work also reported that the entry of magnesium ions from implants into the sensory nerve fiber endings stimulated the release of α-CGRP from dorsal root ganglion, thereby contributing to marked enhancement of osteogenic differentiation capability of osteoprogenitors via cAMP/CREB signaling pathway (*12*). Consistently, we verified the pro-osteogenic effects of CGRP on BMSCs from mice, human, and rats (figs. S4 and S5) and further delineated the key components of PKA/CREB/JUNB signaling axis. A recent reported neuropeptide, neuropeptide Y, under the control of autonomic nervous system, also regulated osteogenic differentiation of BMSC through modulation of cAMP/PKA/CREB/JUNB signaling (*33*), indicating the critical role of JUNB in differentiation fate of BMSCs. However, because of a short half-life under physiological condition, the therapeutic potential of CGRP in orthopedics is still limited. Therefore, the gene therapy targeting CGRP receptor *Calcrl* was considered to modulate the tendon-bone healing in mice with ACL reconstruction. We encapsulated adenovirus into newly developed microhydrogels, which was composed of thiolated hyaluronic acid (SH-SA) as the outer layer and poly(ethylene glycol) diacrylate macromer (HB-PEGDA) as the core through droplet microfluidic fabrication method. As expected, the adenovirus loaded microhydrogels displayed excellent cytocompatibility. The microhydrogels, which were degraded within 24 days

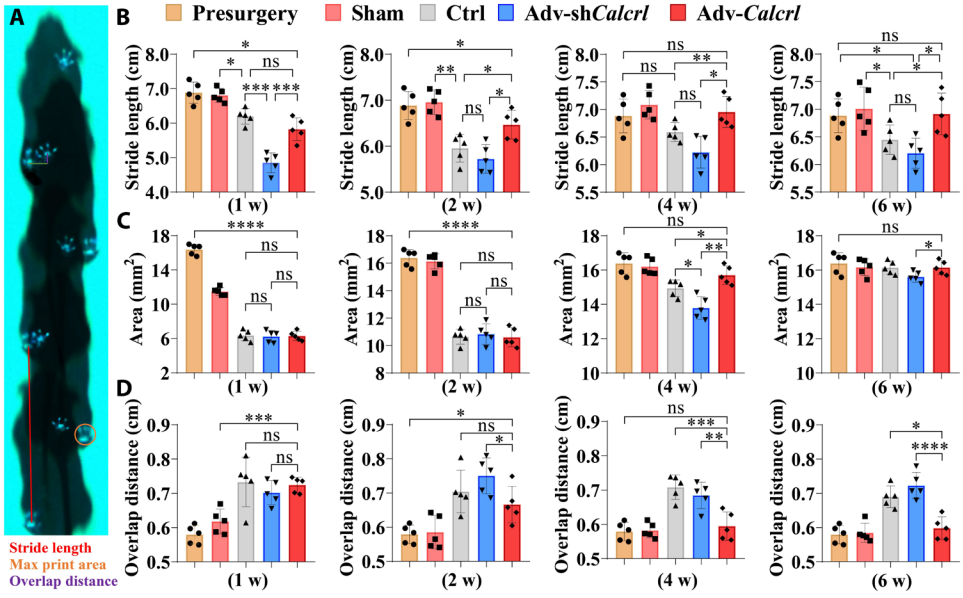

Fig. 9. Gait analysis of mice with various treatment after ACL reconstruction. (**A**) Schematic illustration showing measurement of gait parameters. (**B** to **D**) Quantification of hind-paw stride length, paw print area, and overlap distance in mice with various treatment at 1, 2, 4, and 6 weeks after surgery. *$P < 0.05$, **$P < 0.01$, ***$P < 0.001$, and ****$P < 0.0001$; $n = 5$.

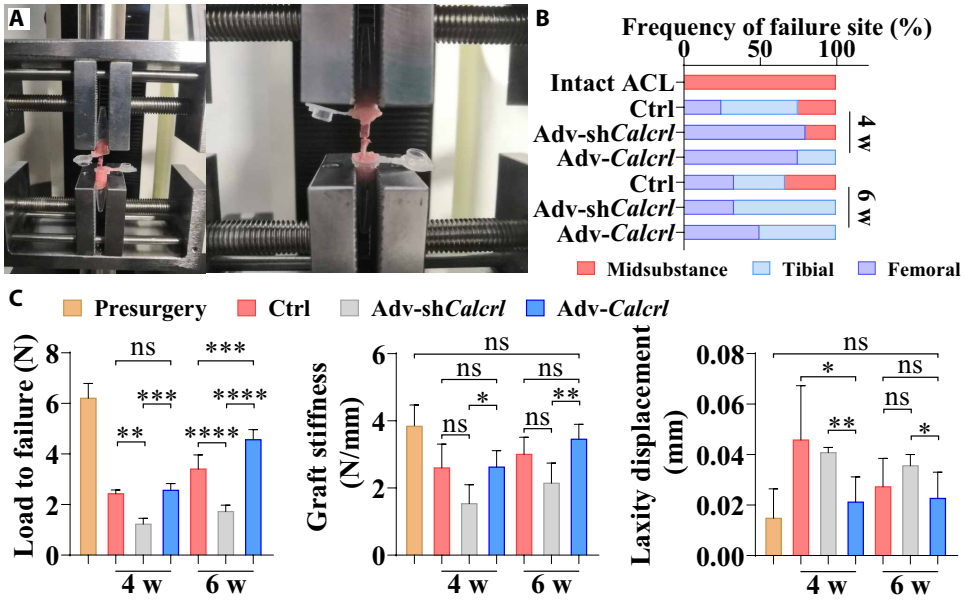

Fig. 10. Mechanical examination of the FTGTC in mice under various treatment. (**A**) The fixation of femur–tendon graft–tibia complex (FTGTC) in the customized jigs for dynamic laxity and tensile testing. (**B**) The failure mode of FTGTC in different groups. (**C**) Quantification of maximum load to failure, graft stiffness, and laxity displacement of FTGTC in different groups at 4 and 6 weeks after surgery. *$P < 0.05$, **$P < 0.01$, ***$P < 0.001$, and ****$P < 0.0001$; $n = 3$ to 5.

in mice (fig. S10), markedly extended the release of adenovirus and reduced the degradation of the shuttle plasmid, contributing to a prolonged while effective in situ dose in bone tunnels for gene transfection.

As the CGRP-containing nerve fibers distribute abundantly in bone marrow (*12*), indicating that the overexpression of CGRP receptor via adenoviral-mediated gene transfer may be an effective adjunct therapy in ACL reconstruction. Consistently, the activation of CGRP receptor–medicated signaling significantly favored the bony ingrowth into the graft and also significantly increased histologic scores in terms of multiple indices, including cellularity, cellular morphology of interface tissue, extent fibrocartilage tissue, interface tissue transition from bone to tendon, and tidemark. In addition to histological evidence, the morphometric measurement of the intra-tunnel bone by micro-CT also validated the treatment efficacy of adv-*Calcrl* transfection in ACL reconstruction. Clinically, the tunnel enlargement and

the peri-tunnel bone loss are frequently encountered phenomenon (*34*, *35*) and increase the risk of knee laxity and revision surgery due to the impairment of tendon-bone fixation and integration. Apparently, the bone tunnel widening was significantly reduced and even prevented in the adv-*Calcrl* group as compared to the other two groups. Meanwhile, the local injection of adv-*Calcrl* also significantly increased intra-tunnel bone mass relative to the other two groups. Therefore, we got the solid evidence that the activation of CGRP receptor–mediated signaling significantly promoted the graft healing through enhancing bone regeneration at the TBI. However, we are still not clear about the repair mechanism: pro-osteogenesis alone or some biological process–mediated pro-osteogenesis?

The promotion of osteogenic differentiation capability of BMSCs in bone marrow would increase the number of osteoblasts, evidenced by more $RUNX2^+$ bone adjacent to the graft in the adv-*Calcrl* group relative to that in the control and adv-sh*Calcrl* groups. In line with in vitro results, the adv-*Calcrl* group showed higher levels of JUNB at the peri-tunnel region relative to the other two groups. The activation of cAMP/PKA/CREB/JUNB signaling leads to production of more osteoblasts, which may exert more effects beyond the components of newly formed bone. Most recently, osteoblast secreted SLIT3 and SHH have been reported to exhibit unique role in promoting type H vessel formation (*36*) and sensory nerve fiber outgrowth (*26*, *28*), respectively. Notably, on one hand, osteoblasts favor expansion of $CD31^{hi}EMCN^{hi}$ endothelial cells through secretion of angiocrine factors in a paracrine manner (*29*). On the other hand, type H blood vessels have a dense arrangement of $RUNX2^+$ osteoprogenitors (*11*), indicating improved ability for bone regeneration. In addition, crosstalk between bone and nerves is also critical during bone modeling and remodeling (*37*). For instance, osteoblast-derived SHH may drive sensory axon growth (*38*), while the newly formed sensory nerve fiber endings release pro-osteogenic neurotransmitters, such as CGRP, leading to increased number of osteoblasts. Therefore, the osteogenesis-angiogenesis and osteogenesis-innervation coupling effects may play a pivotal role in the tendon-bone healing. Encouragingly, compared to the control and adv-sh*Carcrl* groups, the adv-*Calcrl* group showed significant increase in expression of $CGRP^+NF200^+$ and $CD31^{hi}EMCN^{hi}$ around the tendon graft, indicating promoted innervation and more type H vessels at the TBI. Of note, compared to the control group, the adv-*Calcrl* group showed significantly increased fluorescence intensity of CD31, NF200, and RUNX2 at the TBI at different time points, indicating enhanced angiogenesis, innervation, and osteogenesis after activation of CGRP receptor–mediated signaling (fig. S11). In addition, the Manders' colocalization coefficient (MCC) is a metric to describe co-occurrence, so the fraction of one protein that colocalizes with the other can be calculated (*39*). MCC analysis showed 14% of CALCRL overlapping CD31, 13% of CALCRL overlapping NF200, and 27% of CALCRL overlapping RUNX2 in the control group at 1 week after surgery. Notably, 14% of CALCRL overlapping CD31, 15% of CALCRL overlapping NF200, and 37% of CALCRL overlapping RUNX2 were observed after adv-*Calcrl* treatment at 1 week after surgery, indicating that the predominant cell type transfected by adenoviral vector expressing *Calcrl* gene was osteoprogenitor cells. Consistently, the fractions of CALCRL overlapping RUNX2 were still significantly higher than the fractions of CALCRL overlapping CD31 or NF200 in the adv-*Calcrl* group at 2, 4, and 6 weeks after surgery. To our best knowledge, it is the first attempt to investigate the osteoblast-driven innervation and angiogenesis at the TBI. As expected, we observed the activation of CGRP receptor–mediated signaling simultaneously increased type H vessel formation and sensory nerve fiber regeneration, which was also accompanied by the enhanced bony ingrowth toward the TBI. However, there was still lack of direct evidence showing the individual effects of the $CD31^{hi}EMCN^{hi}$ endothelium and sensory nerve axons on the osteogenic differentiation capability of osteoblast precursors at the TBI.

Apart from histological and radiographic assessment, gait characteristics and the tendon-bone bonding strength are also the key indices for evaluation of graft healing quality. Generally, better gait performance may indicate potential for patients returning to activity earlier and lower risk of development and progression of knee osteoarthritis (*40*). Stride length is the distance covered in one gait cycle and defined as the anterior-posterior distance from heel strike to heel strike of the same foot (*41*). The stride length, as one of key gait parameters related to gait speed, is significantly lower in patients with knee dysfunction (*42*). The pain at the surgical wound area (the predrilled bone tunnels and other incisions in soft tissue) may be the predominant cause affecting the stride length in mice at the early healing stage (*43*), so we observed a significant decrease in the stride length in mice at 1 and 2 weeks after surgery no matter what treatment was applied. In addition, the knee laxity also affected the stride length (*44*). As the adv-*Calcrl* treatment significantly enhanced the tendon-bone healing and reduced the knee laxity, the stride length was significantly higher in the adv-*Calcrl* group compared to that in the control group at 2 weeks after surgery. The wound healing at the late stage, e.g., 4 and 6 weeks after operation, can markedly reduce pain, which may profoundly restore the stride length in mice with ACL reconstruction. Of note, the knee stability rather than pain may be the main factor affecting the stride length in mice at the late healing stage. Consistently, we observed that the stride length was significantly higher in the adv-*Calcrl* group relative to that in the control group at 4 and 6 weeks after surgery. Foot (paw) print area or pressure, as one of important gait parameters involving pain, is significantly reduced in patients (mice) with ACL injury (*25*, *45*). The paw overlap distance, defined as the average overlapping distance of ipsilateral paws across successive strides, is significantly increased in animals with knee or ankle surgeries (*46*). Similarly, we found that the wound pain and knee stability affected the values of the two gait parameters, so they showed different characteristics at the early and late healing stages.

Then, to verify whether enhanced tendon graft–bone integration could contribute to improved biomechanical performance, the dynamic laxity assessment and tensile testing were conducted in the FTGTC samples. As expected, the activation of CGRP receptor–mediated signaling significantly reduced knee laxity and improved the maximal failure load relative to the control group. The maximum load to failure was dependent on the integrity of the graft mid-substance and the TBI healing quality. Apparently, the adv-sh*Calcrl* deteriorated the tendon-bone healing, which may simultaneously induce graft laxity, so we observed that the load to failure was significantly lower in the adv-sh*Calcrl* group relative to that in the control group and the adv-*Calcrl* group. The graft healing was continuously promoted over healing time especially in the adv-*Calcrl* group according to the histologic scores, thereby contributing to significantly higher load to failure in the adv-*Calcrl* group compared to the other two groups at 6 weeks after surgery. The laxity displacement may be primarily dependent on the tendon-bone healing quality. Therefore, the dynamic knee laxity measurement showed that the displacement was lowest in the adv-*Calcrl* group relative to the other two groups at 4 weeks after surgery.

Although the displacement was still lower in the adv-*Calcrl* group relative to that in the control group at 6 weeks after surgery, there was no significant difference, indicating the important role of adv-*Calcrl* in accelerating tendon-bone healing.

Meanwhile, we observed the failure mode located at the bone insertions in the adv-*Calcrl* group. Generally, impaired tendon-bone healing may lead to slippage of the tendon graft from the bone tunnels under cyclic loading during walking, thereby causing knee laxity, which would then induce the degeneration of graft mid-substance due to the lack of loading (*47*, *48*). This would deteriorate the mechanical strength of the graft mid-substance. Of note, as the TBI healing is also impaired, there are chances for both graft mid-substance and the TBI as the biomechanical failure site. Enhanced tendon-bone healing would reduce slippage of the tendon graft from the bone tunnels under loading, which can dampen the degeneration of the graft mid-substance and thereby maintain its mechanical strength. At such circumstance, there are also possibilities for both graft mid-substance and the TBI as the biomechanical failure site. Together, the two functional assessment outcomes validated that accelerated and promoted graft healing into bone tunnels favors gait performance and activity recovery, which are critical cues for patients during rehabilitation.

Above all, we developed a delivery system for gene therapy targeting CGRP receptor in bone tunnels, aiming to stimulate osteogenesis-angiogenesis and osteogenesis-innervation coupling effects for promoted osseous ingrowth toward the TBI after ACL reconstruction (fig. S12).

However, there are still some limitations and concerns required to address in the future work. First, there would be concerns on the short observation period in mice. It is crucial to perform the study with a long-term period, which may provide a more convincing evidence to demonstrate the clinical potential of such strategy. As reported in the literatures, the cancellous bone turnover in mice is ~0.7% per day while 0.1% per day measured in humans (*49*). The bone remodeling period is about 2 weeks in mice while 6 to 9 months in humans (*50*). Here, we considered an observation period of 6 weeks in mice, which may be equivalent to 1 year or even longer period in humans. In clinics, the fibrous interface was in continuous contact with the osteoid tissue and Sharpey-like fibers started to penetrate into the surrounding bone tissue at 6 months after surgery. At 10 months, mature indirect anchorage was obtained (*51*). We extended the observation time to 8 weeks and found that there was no significant difference in the tendon-bone healing quality in mice (6 weeks versus 8 weeks) (fig. S13), indicating the entry of mature healing stage at 6 weeks in mice with ACL reconstruction. Second, as a neurotransmitter, CGRP is also a mediator of angiogenesis (*52*), so the activation of CGRP receptor–mediated signaling may simultaneously affect the formation of blood vessels. Nevertheless, although the predominant cell type transfected by adenoviral vectors expressing *shCalcrl* or *Calcrl* genes was osteoprogenitor cells ($RUNX2^+CALCRL^+$), the local injection of adenovirus loaded in HMPs may also transfect other cell types, e.g., endothelial cells and neural cells. Thus, the tissue-specific Cre-driver mice line may be required to exclude the confounding effects. Third, the activation of CGRP receptor–mediated signaling modulated innervation (or $CD31^{hi}EMCN^{hi}$ endothelium) at the TBI. However, it was not clear whether the type H vessel or the innervation at the TBI affects the graft integration toward the bone tunnels. Therefore, it will be significant to investigate the effects of innervation (or type H vessels) on osseous ingrowth at the TBI in the following studies. For instance, SLIT3 or Netrin-1 and their neutralizing antibodies may be considered for injection in tunnels to regulate type H vessel or sensory nerve fiber formation, for further identification of osteogenesis-innervation and osteogenesis-angiogenesis coupling effects during graft healing. Encouragingly, our data revealed that the SLIT3-treated mice, exhibiting improved angiogenesis and innervation at the TBI, showed better gait performance and biomechanical behaviors relative to the control group. Meanwhile, the SLIT3 neutralizing antibody–treated mice showed the opposite results (fig. S14). It indicated the potential correlation between the innervation or angiogenesis and knee function recovery. Fourth, CALCRL interacts with receptor activity-modifying protein-1 (RAMP1) to generate a CGRP receptor. It is unclear about the role of RAMP1 in the tendon-bone healing in mice after adv-*Calcrl* or adv-sh*Calcrl* treatment, which is an interesting and important topic to broaden our understanding of the significance of the CGRP receptor–mediated signaling pathway in the tendon-bone healing. Fifth, the biosafety concern may be raised for the gene therapy in the treatment of tendon-bone injuries. We tested the blood hematological parameters of the untreated mice and the treated mice after injection of HMPs loading PBS, scramble shRNA, adv-*Calcrl*, and adv-sh*Calcrl*. As shown in fig. S15A, there was no abnormal alteration in these hematological parameters after adenoviral treatment at the early stage. In addition, compared to the control group, there was no substantial increase of F4/80-positive macrophages around the bone tunnels (fig. S15B), indicating the high biocompatibility of our used adenovirus. However, the observation period for the potential health risks induced by adenovirus treatment was still short, so a long-term assessment period is necessary in the future work. Last, although the adv-*Calcrl* treatment only caused low expression of CALCRL in the tendon graft, the potential effect of CALCRL on the fate of the tendon graft is worthy of investigation.

In conclusion, we found that CGRP promoted osteogenic differentiation capability of BMSCs via activation of cAMP/PKA/CREB/JUNB signaling pathway, which was further evidenced by significantly higher fluorescence intensity of $RUNX2^+$ region at the TBI in the adv-*Calcrl* group relative to that in the control group. Afterward, we prepared a novel microhydrogel to encapsulate adenovirus plasmid for gene therapy, with an extended while more stable in situ release, aiming to modulation of CGRP receptor expression levels in bone tunnels. Encouragingly, the adenoviral plasmid–loaded hydrogels exhibited satisfactory cytocompatibility and gene transfection efficiency. The mice with the local injection of adv-*Calcrl* showed significantly improved graft healing and more intra-tunnel bone mass in terms of histological and radiographic assessment relative to the control and the adv-sh*Calcrl* groups. Simultaneously, the activation of CGRP receptor–mediated signaling also favored the formation of $CGRP^+$ sensory nerve fibers and $CD31^{hi}EMCN^{hi}$ endothelium at the TBI, which was accompanied by improved gait characteristics and biomechanical performance. Collectively, the activation of CGRP receptor–mediated signaling is a potential therapeutic method to modify the tendon-bone healing in patients.

MATERIALS AND METHODS

Fabrication of HMPs

To prepare the HMPs, a microfluidic droplet maker was fabricated via soft lithography by pouring poly(dimethylsiloxane) along with cross-linker (Sylgard 184 elastomer kit, Dow Corning; pre-polymer:cross-linker, 12: 1) onto a silicon wafer patterned with SU-8 photoresist (*53*). Then, in a typical experiment, aqueous dispersions containing 1% (w/v) SH-HA, 3.33% (w/v) HB-PEGDA, and adenovirus (3.52 ×

10^9 IFU/ml) were intersected by the fluorinertTM FC-40 oil containing 2 wt % Pico-SurfTM in the microfluidic droplet maker to generate uniform microdroplets. The collected microdroplets were left at room temperature for 6 hours to ensure sufficient gelation and the formation of HMPs. Last, to purify the HMPs, 20% v/v 1H,1H,2H,2H-perfluoro-1-octanol in Novec 7500 oil was added into the samples to remove the surfactant.

Encapsulation of adenovirus in micro-hydrogel for controlled release

The adenovirus plasmids were designed (fig. S1) and tried the transfection efficiency in BMSCs via detection of GFP as a reporter (fig. S2). The adenoviral vectors loaded in the HMPs with a titer fixed at 4.5×10^{10} IFU/ml were dissolved in the PBS solution at 37°C environment. At different time points, referring to 0, 1, 3, 5, 7, and 9 days, a certain volume (5 μl) of the mixed solution was collected and centrifuged for measurement of the amount of adenovirus by real-time qPCR analysis using ABI-7500 (Applied Biosystems, Foster City, CA, USA). Similarly, the adenoviral vectors alone were set as the control for comparison.

Cytocompatibility assessment

BMSCs were isolated from 3- to 5-week-old male C57BL/6J mice (*54*). All cells were cultured in Dulbecco's modified Eagle's medium (Gibco) supplemented with 15% fetal bovine serum (Gibco) and 1% penicillin-streptomycin at 37°C in a humidified atmosphere containing 5% CO_2. BMSCs at passage 2 were seeded in 96-well plate and cultured with gradient concentration HMPs for 24 or 48 hours; then, the cytotoxicity of HMPs was evaluated by the CCK-8 (GlpBio, USA). In terms of the Live/Dead assay (Live/Dead cell imaging kit, US Everbright Inc., China), the BMSCs at passage 3 were used for measurement of cell viability after incubation with different concentrations of HMPs.

Osteogenic differentiation

Mouse, rat, and human BMSCs at passage 3 or 4 were seeded in a six-well plate at a density of 1×10^5 cells per well. Osteogenic differentiation was induced in the osteogenic induction medium (OIM), which was composed of basic growth medium supplemented with 100 nM dexamethasone (Sigma-Aldrich, USA), 10 mM sodium β-glycerophosphate (Sigma-Aldrich, USA), and 50 μM ascorbic acid (Sigma-Aldrich, USA). The culture medium was changed every 3 days. Real-time qPCR (table S1) and Western blot analysis were used for examination of expression levels of osteogenic markers in noninduced BMSCs (Blank) and induced BMSCs, which were incubated in OIM with or without addition of CGRP and H-89 (inhibitor of PKA) for 3, 7, and 14 days, respectively. In addition, the presence of calcium nodules in BMSCs on days 14 and 21 after osteogenic differentiation was observed by Alizarin Red S staining and then quantitatively analyzed by applying 10% cetylpyridinium chloride (Sigma-Aldrich, USA) for dissolution for 15 min at 560 nm.

Animals for ACL reconstruction

Ten- to 12-week-old male C57BL/6J mice were provided by the Laboratory Animal Research Center of Sun Yat-Sen University. All the operations were performed with the approval by the local Animal Care and Use committee (SYSU-IACUC-2020-B0858). All mice were housed in a specific pathogen–free animal facility with free access to water and laboratory chow. The room is maintained at a controlled temperature (23° ± 2°C) and humidity (40 ± 5%). As shown in fig. S3 (A and B), the surgery was performed according to our previously reported protocol (*55*). Briefly, after appropriate anesthesia (1% sodium pentobarbital, 0.06 ml/10 g body weight), a 3- to 5-mm incision was made in the medial skin of left hindlimb to expose the Achilles tendon and harvest the medial gastrocnemius tendon with a high-tension suture (Ethicon 8-0) fixed at both ends. The isolated tendon graft was then temporarily stored in PBS. Afterward, an incision was made adjacent to the patellar tendon to allow the patellar bone dislocation before the creation of bone tunnel of 0.5 mm in diameter using a bone drill along the footprints of ACL through transtibial technique. Then, the micro-hydrogels with or without Adv-sh*Calcrl* or Adv-*Calcrl* loading was injected into the predrilled femoral and tibial tunnels after the transection of the native ACL. As the direct placement of the tendon graft into the bone tunnel would cause the loss of the injected micro-hydrogels, the tendon graft stored in PBS was then transferred to the micro-hydrogels with or without adenovirus loading, which may favor adenovirus compensation. After the insertion of the tendon graft into the bone tunnel, both of the graft ends were sutured tightly with surrounding tissues in both femoral and tibial sides. During the tendon graft fixation at the tibial entrance, a constant force of ~0.1 N was applied to keep the graft tension. Last, the patellar bone was relocated to facilitate a layer-by-layer closure in incisions with absorbable sutures (Ethicon 8-0). In addition, the animal number assigned for different testings in each group at the indicated time points was described in fig. S3C. Of note, G.W. prepared the micro-hydrogels with or without Adv-sh*Calcrl* or Adv-*Calcrl* loading and then labeled them with different alphabet letters, e.g., A, B, and C, for the following use. X.Z. was blinded to the identity of those letter labeled samples, which were then used for animal experiments by him.

Western blot analysis

Cells were lysed using radioimmunoprecipitation assay (Solarbio) containing protease phosphatase inhibitor cocktail (Solarbio) for protein extraction. Protein lysates (20 μg) were separated by SDS–polyacrylamide gel electrophoresis and transferred to polyvinylidene difluoride membranes for antibody incubation. After blocked with Tris-buffered saline, 0.1% Tween 20 (TBST) containing 5% skim milk powder, the membrane was probed overnight with primary antibodies at 4°C and washed with TBST. After that, the membranes were incubated with secondary antibodies at room temperature for 1 hour. Afterward, the protein bands were visualized using the ECL kit (Monad) and recorded with the Alpha-FluorChemQ imaging system.

The following primary antibodies were used: RUNX2 (sc-390351, Santa Cruz Biotechnology), OSX (ab209484, Abcam), CREB (381013, ZenBio), p-CREB (380697, ZenBio), JUNB (sc-8051, Santa Cruz Biotechnology), PKA (251816, ZenBio), CALCRL (bs-1860R, Bioss), RAMP1 (R25544, ZenBio), SHH (BF0146, Affinity), and glyceraldehyde-3-phosphate dehydrogenase (BS65483M, BIOGOT; 380626, ZenBio). The following secondary antibodies were used: goat anti-mouse immunoglobulin G (IgG) H&L [horseradish peroxidase (HRP)] (511103, ZenBio) and goat anti-rabbit IgG H&L (HRP) (511203, ZenBio).

Tissue collection

Animals were anesthetized with sodium pentobarbital at 2, 4, and 6 weeks after surgery. Trans-cardiac perfusion was performed with saline containing 4% paraformaldehyde and 0.1% sodium heparin

(*56*). Afterward, the operative femoral-tendon-tibial complex was completely isolated, then wrapped with saline gauze, and lastly stored at −80°C for micro-CT scanning, biomechanical testing, and histological analysis.

Histological analysis

After fixation in 4% paraformaldehyde for 24 to 48 hours, the knee joints were decalcified in 15% EDTA tetrasodium solution. After 4 weeks, the decalcified tissues were dehydrated through an ascending series of ethanol, cleared twice in xylene, and embedded in optimal cutting temperature compound (4583, Tissue-Tek) and frozen in cryostat (CM1950, Leica). The embedded samples were sectioned at 7-μm thickness along the coronal plate from anterior to posterior before H&E and Safranin O/Fast Green staining for histological assessment (table S2). The microscopic images were acquired using a microscope (BDS400, CQOPTEC).

For immunofluorescence, the frozen tissue sections with 20 μm were transferred directly into antigen retrieval solution (sodium citrate, pH 6.0). Then, the sections were blocked with the mixture of 3% goat serum, 1% bovine serum albumin, and 0.1% Triton X-100 in PBS for 1 hour at room temperature. Subsequently, the sections were probed overnight with primary antibodies at 4°C and then incubated with the secondary antibodies at room temperature for 1 hour. Nuclei were stained with 4′,6-diamidino-2-phenylindole, and the images were recorded using a confocal laser scanning microscope (FV3000, Olympus). The following primary antibodies were used: RUNX2 (sc-390351, Santa Cruz Biotechnology), CALCRL (bs-1860R, Bioss), JUNB (sc-8051, Santa Cruz Biotechnology), SHH (BF0146, Affinity), CGRP (sc-57053, Santa Cruz Biotechnology), NF200 (ab207176, Abcam), CD31 (AM32708PU-N, ORIGENE), and EMCN (bs6884R, Bioss), and SLIT3 (DF9909, Affinity). The following secondary antibodies were used: goat anti-rabbit IgG(H+L) DyLight 488 (BS10017, Bioworlde), goat anti-rabbit IgG(H+L) Dylight 649 (A23620, Abbkine), goat anti-mouse IgG(H+L) Dylight 488 (BS21846, Bioworlde), and goat anti-mouse IgG (H+L) Dylight 649 (A23610, Abbkine).

Gait analysis

The gait analysis was performed according to our previous protocol (*57*). Briefly, all the mice were equally adapted to walk across a runway, 40-cm long and 5-cm wide, for 5 min in the dark. All the mice walk freely and as straight as possible. The footprint was recorded by a high-speed video camera that was position under the glass walkway (RunwayScan, CleverSys Inc). Gait parameters (stride length, paw print area, and overlap distance) were measured for comparison.

Biomechanical tests

After the removal of all the soft tissue but not the reconstructed tendon graft, the femur-tendon-tibia complex was fixed in a 0.5-ml centrifuge tube with denture base resins. The assessment of dynamic joint laxity was performed with the knee in full extension at a speed of 2 mm/min in a cyclic loading model between 0.1 and 1 N on a mechanical testing machine (ZQ-990LB, Zhiqu Precision Instrument). After 10 cycles, the resultant displacement was recorded in mm. After the laxity test, the tensile test for the maximum load to failure was conducted at a speed of 2 mm/min until an abrupt drop in loading curve. The maximal load and the model of failure were recorded. The stiffness was calculated at linear region of the load-displacement curve.

Micro-CT analysis

The knee joint tissue was fixed in 4% paraformaldehyde for 24 hours at room temperature and stored in 70% ethanol. After fixed in scan tube, the samples were scanned with a voltage, a current, and an integration time set as 70 kV, 114 μA, and 230 ms, respectively (SCANCO μCT 100, SCANCO Medical AG). For accurate images of trabecular microstructure, including BMD, BV/TV, Tb. N, Tb. Th, Tb. Sp, and Tb. Th, in a round tunnel of 0.5 mm in diameter, an isotropic voxel size of 9 μm was applied.

Statistical analysis

All data are expressed as means ± SD. GraphPad Prism 8 software was used for data processing, statistical analysis, and drawing. The number of biological replicates was at least 3. Independent Student's *t* test was used for comparison of data between two groups, while one-way analysis of variance (ANOVA) with Scheffe post hoc test was applied for multiple comparisons. The Kruskal-Wallis test was used for multiple comparisons of data from the semiquantitative analysis of the tendon-bone healing quality. The significant level was set as 0.05, and the statistical significance was declared as (*) at $P < 0.05$, (**) at $P < 0.01$, and (***) at $P < 0.001$. The load to failure was set as the primary outcome for the calculation of the sample size when the values of type I error α and power (1-β) were set as 0.05 and 0.8, respectively. Therefore, 121 mice in total were used for gait analysis, histological assessment, radiographic evaluation, and mechanical testing in this study.

Supplementary Materials

This PDF file includes:

Figs. S1 to S15
Tables S1 and S2

REFERENCES AND NOTES

1. S. L. Sherman, J. Calcei, T. Ray, R. A. Magnussen, V. Musahl, C. C. Kaeding, M. Clatworthy, J. A. Bergfeld, M. P. Arnold, ACL Study Group presents the global trends in ACL reconstruction: Biennial survey of the ACL Study Group. *J. ISAKOS* **6**, 322–328 (2021).
2. P. A. Renstrom, Eight clinical conundrums relating to anterior cruciate ligament (ACL) injury in sport: Recent evidence and a personal reflection. *Br. J. Sports Med.* **47**, 367–372 (2013).
3. S. N. Crawford, B. R. Waterman, J. H. Lubowitz, Long-term failure of anterior cruciate ligament reconstruction. *Art Ther.* **29**, 1566–1571 (2013).
4. S. Patel, J. M. Caldwell, S. B. Doty, W. N. Levine, S. Rodeo, L. J. Soslowsky, S. Thomopoulos, H. H. Lu, Integrating soft and hard tissues via interface tissue engineering. *J. Orthop. Res.* **36**, 1069–1077 (2018).
5. B. B. Rothrauff, A. Jorge, D. de Sa, J. Kay, F. H. Fu, V. Musahl, Anatomic ACL reconstruction reduces risk of post-traumatic osteoarthritis: A systematic review with minimum 10-year follow-up. *Knee Surg. Sports Traumatol. Arthrosc.* **28**, 1072–1084 (2020).
6. K. Kang, Q. Geng, L. Cui, L. Wu, L. Zhang, T. Li, Q. Zhang, S. Gao, Upregulation of Runt related transcription factor 1 (RUNX1) contributes to tendon-bone healing after anterior cruciate ligament reconstruction using bone mesenchymal stem cells. *J. Orthop. Surg. Res.* **17**, 266 (2022).
7. P. Y. Mengsteab, T. Otsuka, A. McClinton, N. S. Shemshaki, S. Shah, H. M. Kan, E. Obopilwe, A. T. Vella, L. S. Nair, C. T. Laurencin, Mechanically superior matrices promote osteointegration and regeneration of anterior cruciate ligament tissue in rabbits. *Proc. Natl. Acad. Sci. U.S.A.* **117**, 28655–28666 (2020).
8. A. T. Hexter, T. Thangarajah, G. Blunn, F. S. Haddad, Biological augmentation of graft healing in anterior cruciate ligament reconstruction: A systematic review. *Bone Joint J.* **100-B**, 271–284 (2018).
9. S. K. Ramasamy, A. P. Kusumbe, L. Wang, R. H. Adams, Endothelial Notch activity promotes angiogenesis and osteogenesis in bone. *Nature* **507**, 376–380 (2014).
10. A. P. Kusumbe, S. K. Ramasamy, R. H. Adams, Coupling of angiogenesis and osteogenesis by a specific vessel subtype in bone. *Nature* **507**, 323–328 (2014).
11. Y. Peng, S. Wu, Y. Li, J. L. Crane, Type H blood vessels in bone modeling and remodeling. *Theranostics* **10**, 426–436 (2020).

12. Y. Zhang, J. Xu, Y. C. Ruan, M. K. Yu, M. O'Laughlin, H. Wise, D. Chen, L. Tian, D. Shi, J. Wang, S. Chen, J. Q. Feng, D. H. Chow, X. Xie, L. Zheng, L. Huang, S. Huang, K. Leung, N. Lu, L. Zhao, H. Li, D. Zhao, X. Guo, K. Chan, F. Witte, H. C. Chan, Y. Zheng, L. Qin, Implant-derived magnesium induces local neuronal production of CGRP to improve bone-fracture healing in rats. *Nat. Med.* **22**, 1160–1169 (2016).
13. B. Ji, Y. Zhao, A. Esteve-Nunez, R. Liu, Y. Yang, A. Nzihou, Y. Tai, T. Wei, C. Shen, Y. Yang, B. Ren, X. Wang, Y. Wang, Where do we stand to oversee the coronaviruses in aqueous and aerosol environment? Characteristics of transmission and possible curb strategies. *Chem. Eng. J.* **413**, 127522 (2021).
14. H. Chen, H. Lu, J. Huang, Z. Wang, Y. Chen, T. Zhang, Calcitonin gene-related peptide influences bone-tendon interface healing through osteogenesis: Investigation in a rabbit partial patellectomy model. *Orthop. J. Sports Med.* **9**, 23259671211003982 (2021).
15. A. Kumar, J. D. Potts, D. J. DiPette, Protective role of α-calcitonin gene-related peptide in cardiovascular diseases. *Front. Physiol.* **10**, 821 (2019).
16. N. K. Y. Wee, S. Novak, D. Ghosh, S. H. Root, I. M. Dickerson, I. Kalajzic, Inhibition of CGRP signaling impairs fracture healing in mice. *J. Orthop. Res.* **41**, 1228–1239 (2023).
17. Y. Song, G. X. Han, L. Chen, Y. Z. Zhai, J. Dong, W. Chen, T. S. Li, H. Y. Zhu, The role of the hippocampus and the function of calcitonin gene-related peptide in the mechanism of traumatic brain injury accelerating fracture-healing. *Eur. Rev. Med. Pharmacol. Sci.* **21**, 1522–1531 (2017).
18. J. Appelt, A. Baranowsky, D. Jahn, T. Yorgan, P. Kohli, E. Otto, S. K. Farahani, F. Graef, M. Fuchs, A. Herrera, M. Amling, T. Schinke, K. H. Frosch, G. N. Duda, S. Tsitsilonis, J. Keller, The neuropeptide calcitonin gene-related peptide alpha is essential for bone healing. *EBioMedicine* **59**, 102970 (2020).
19. L. Li, A. Kreicbergs, J. Bergström, A. Stark, M. Ahmed, Site-specific CGRP innervation coincides with bone formation during fracture healing and modeling: A study in rat angulated tibia. *J. Orthop. Res.* **25**, 1204–1212 (2007).
20. I. Pountos, M. Panteli, A. Lampropoulos, E. Jones, G. M. Calori, P. V. Giannoudis, The role of peptides in bone healing and regeneration: A systematic review. *BMC Med.* **14**, 103 (2016).
21. G. N. Onuoha, Circulating sensory peptide levels within 24 h of human bone fracture. *Peptides* **22**, 1107–1110 (2001).
22. Y. Yamada, A. Ohazama, T. Maeda, K. Seo, The Sonic Hedgehog signaling pathway regulates inferior alveolar nerve regeneration. *Neurosci. Lett.* **671**, 114–119 (2018).
23. K. Matsumoto, T. Shimo, N. Kurio, T. Okui, K. Obata, M. Masui, P. Pang, Y. Horikiri, A. Sasaki, Expression and role of sonic hedgehog in the process of fracture healing with aging. *In Vivo* **30**, 99–105 (2016).
24. W. Qiao, D. Pan, Y. Zheng, S. Wu, X. Liu, Z. Chen, M. Wan, S. Feng, K. M. C. Cheung, K. W. K. Yeung, X. Cao, Divalent metal cations stimulate skeleton interoception for new bone formation in mouse injury models. *Nat. Commun.* **13**, 535 (2022).
25. S. Zhu, J. Zhu, G. Zhen, Y. Hu, S. An, Y. Li, Q. Zheng, Z. Chen, Y. Yang, M. Wan, R. L. Skolasky, Y. Cao, T. Wu, B. Gao, M. Yang, M. Gao, J. Kuliwaba, S. Ni, L. Wang, C. Wu, D. Findlay, H. K. Eltzschig, H. W. Ouyang, J. Crane, F. Q. Zhou, Y. Guan, X. Dong, X. Cao, Subchondral bone osteoclasts induce sensory innervation and osteoarthritis pain. *J. Clin. Invest.* **129**, 1076–1093 (2019).
26. N. C. Bambakidis, X. Wang, R. J. Lukas, R. F. Spetzler, V. K. Sonntag, M. C. Preul, Intravenous hedgehog agonist induces proliferation of neural and oligodendrocyte precursors in rodent spinal cord injury. *Neurosurgery* **67**, 1709–1715 (2010).
27. Q. Q. Wan, W. P. Qin, M. J. Shen, Y. X. Ma, B. Li, S. Y. Liu, F. R. Tay, K. Jiao, L. N. Niu, Simultaneous regeneration of bone and nerves through materials and architectural design: Are we there yet? *Adv. Funct. Mater.* **30**, 2003542 (2020).
28. J. R. Sims, S. W. Lee, K. Topalkara, J. Qiu, J. Xu, Z. Zhou, M. A. Moskowitz, Sonic hedgehog regulates ischemia/hypoxia-induced neural progenitor proliferation. *Stroke* **40**, 3618–3626 (2009).
29. R. Xu, A. Yallowitz, A. Qin, Z. Wu, D. Y. Shin, J. M. Kim, S. Debnath, G. Ji, M. P. Bostrom, X. Yang, C. Zhang, H. Dong, P. Kermani, S. Lalani, N. Li, Y. Liu, M. G. Poulos, A. Wach, Y. Zhang, K. Inoue, A. Di Lorenzo, B. Zhao, J. M. Butler, J. H. Shim, L. H. Glimcher, M. B. Greenblatt, Targeting skeletal endothelium to ameliorate bone loss. *Nat. Med.* **24**, 823–833 (2018).
30. J. Zhang, H. Y. Yong, S. A, Q. Xu, Y. P. Miao, J. Lyu, Y. S. Gao, M. Zeng, D. Z. Zhou, Z. Y. Yu, H. Y. Tai, W. X. Wang, Structural design of robust and biocompatible photonic hydrogels from an in situ cross-linked hyperbranched polymer system. *Chem. Mater.* **30**, 6091–6098 (2018).
31. S. J. Kim, J. H. Bae, S. H. Song, H. C. Lim, Bone tunnel widening with autogenous bone plugs versus bioabsorbable interference screws for secondary fixation in ACL reconstruction. *J. Bone Joint Surg. Am.* **95**, 103–108 (2013).
32. M. G. Rosenfeld, J. J. Mermod, S. G. Amara, L. W. Swanson, P. E. Sawchenko, J. Rivier, W. W. Vale, R. M. Evans, Production of a novel neuropeptide encoded by the calcitonin gene via tissue-specific RNA processing. *Nature* **304**, 129–135 (1983).
33. Y. Zhang, C. Y. Chen, Y. W. Liu, S. S. Rao, Y. J. Tan, Y. X. Qian, K. Xia, J. Huang, X. X. Liu, C. G. Hong, H. Yin, J. Cao, S. K. Feng, Z. H. He, Y. Y. Li, Z. W. Luo, B. Wu, Z. Q. Yan, T. H. Chen, M. L. Chen, Y. Y. Wang, Z. X. Wang, Z. Z. Liu, M. J. Luo, X. K. Hu, L. Jin, T. F. Wan, T. Yue, S. Y. Tang, H. Xie, Neuronal induction of bone-fat imbalance through osteocyte neuropeptide Y. *Adv. Sci.* **8**, e2100808 (2021).
34. T. C. Wilson, A. Kantaras, A. Atay, D. L. Johnson, Tunnel enlargement after anterior cruciate ligament surgery. *Am. J. Sports Med.* **32**, 543–549 (2004).
35. P. P. Lui, Y. W. Lee, T. Y. Mok, Y. C. Cheuk, Local administration of alendronate reduced peri-tunnel bone loss and promoted graft-bone tunnel healing with minimal systemic effect on bone in contralateral knee. *J. Orthop. Res.* **31**, 1897–1906 (2013).
36. N. Li, K. Inoue, J. Sun, Y. Niu, S. Lalani, A. Yallowitz, X. Yang, C. Zhang, R. Shen, B. Zhao, R. Xu, M. B. Greenblatt, Osteoclasts are not a source of SLIT3. *Bone Res.* **8**, 11 (2020).
37. Q. Q. Wan, W. P. Qin, Y. X. Ma, M. J. Shen, J. Li, Z.-B. Zhang, J.-H. Chen, F. R. Tay, L.-N. Niu, K. Jiao, Crosstalk between bone and nerves within bone. *Science* **8**, 2003390 (2021).
38. L. Leitao, E. Neto, F. Conceicao, A. Monteiro, M. Couto, C. J. Alves, D. M. Sousa, M. Lamghari, Osteoblasts are inherently programmed to repel sensory innervation. *Bone Res.* **8**, 20 (2020).
39. K. W. Dunn, M. M. Kamocka, J. H. McDonald, A practical guide to evaluating colocalization in biological microscopy. *Am. J. Physiol. Cell Physiol.* **300**, C723–C742 (2011).
40. H. F. Hart, A. G. Culvenor, N. J. Collins, D. C. Ackland, S. M. Cowan, Z. Machotka, K. M. Crossley, Knee kinematics and joint moments during gait following anterior cruciate ligament reconstruction: A systematic review and meta-analysis. *Br. J. Sports Med.* **50**, 597–612 (2016).
41. J. A. Roper, M. J. Terza, M. D. Tillman, C. J. Hass, Adaptation strategies of individuals with anterior cruciate ligament reconstruction. *Orthop. J. Sports Med.* **4**, 2325967115627611 (2016).
42. H. Li, S. Hu, R. Zhao, Y. Zhang, L. Huang, J. Shi, P. Li, X. Wei, Gait analysis of bilateral knee osteoarthritis and its correlation with western ontario and mcmaster university osteoarthritis index assessment. *Medicina* **58**, 1419 (2022).
43. T. Histing, A. Kristen, C. Roth, J. H. Holstein, P. Garcia, R. Matthys, M. D. Menger, T. Pohlemann, In vivo gait analysis in a mouse femur fracture model. *J. Biomech.* **43**, 3240–3243 (2010).
44. D. Mandeville, L. R. Osternig, L. S. Chou, The effect of total knee replacement surgery on gait stability. *Gait Posture* **27**, 103–109 (2008).
45. K. Sugawara, K. Okada, I. Saito, A. Saito, M. Wakasa, Foot pressure pattern during walking in individuals with anterior cruciate ligament injury. *J. Am. Podiatr. Med. Assoc.* **106**, 201–206 (2016).
46. J. Li, Z. Chen, Y. Cheng, C. Gao, J. Li, X. Gu, F. He, Z. Luo, H. Yang, H. Zhang, J. Yu, Ligamentous injury-induced ankle instability causing posttraumatic osteoarthritis in a mouse model. *BMC Musculoskelet. Disord.* **23**, 223 (2022).
47. H. Mutsuzaki, H. Nakajima, Y. Wadano, S. Furuhata, M. Sakane, Influence of knee immobilization on chondrocyte apoptosis and histological features of the anterior cruciate ligament insertion and articular cartilage in rabbits. *Int. J. Mol. Sci.* **18**, 253 (2017).
48. N. Andarawis-Puri, E. L. Flatow, L. J. Soslowsky, Tendon basic science: Development, repair, regeneration, and healing. *J. Orthop. Res.* **33**, 780–784 (2015).
49. R. L. Jilka, The relevance of mouse models for investigating age-related bone loss in humans. *J. Gerontol. A Biol. Sci. Med. Sci.* **68**, 1209–1217 (2013).
50. T. Taguchi, M. J. Lopez, An overview of de novo bone generation in animal models. *J. Orthop. Res.* **39**, 7–21 (2021).
51. H. Lu, C. Chen, S. Xie, Y. Tang, J. Qu, Tendon healing in bone tunnel after human anterior cruciate ligament reconstruction: A systematic review of histological results. *J. Knee Surg.* **32**, 454–462 (2019).
52. P. I. Mapp, D. F. McWilliams, M. J. Turley, E. Hargin, D. A. Walsh, A role for the sensory neuropeptide calcitonin gene-related peptide in endothelial cell proliferation in vivo. *Br. J. Pharmacol.* **166**, 1261–1271 (2012).
53. Y. Li, Z. Di, X. Yan, H. Wen, W. Cheng, J. Zhang, Z. Yu, Biocatalytic living materials built by compartmentalized microorganisms in annealable granular hydrogels. *Chem. Eng. J.* **445**, 136822 (2022).
54. M. Soleimani, S. Nadri, A protocol for isolation and culture of mesenchymal stem cells from mouse bone marrow. *Nat. Protoc.* **4**, 102–106 (2009).
55. J. Wang, Y. Wu, H. Li, Y. Liu, X. Bai, W. Chau, Y. Zheng, L. Qin, Magnesium alloy based interference screw developed for ACL reconstruction attenuates peri-tunnel bone loss in rabbits. *Biomaterials* **157**, 86–97 (2018).
56. G. J. Gage, D. R. Kipke, W. Shain, Whole animal perfusion fixation for rodents. *J. Vis. Exp.*, 3564 (2012).
57. H. Yao, J. Xu, J. Wang, Y. Zhang, N. Zheng, J. Yue, J. Mi, L. Zheng, B. Dai, W. Huang, S. Yung, P. Hu, Y. Ruan, Q. Xue, K. Ho, L. Qin, Combination of magnesium ions and vitamin C alleviates synovitis and osteophyte formation in osteoarthritis of mice. *Bioact. Mater.* **6**, 1341–1352 (2021).

Acknowledgments

Funding: This work was supported by the National Key Research and Development Program of China [grant no. 2021YFC2104300 (Z.Y.)], the National Natural Science Foundation of China

[grant nos. 32271381 (J.W.), 52273207 (J.Z.), 32111530117, and 22278214 (Z.Y.)], the Foundation of Guangdong Provincial Key Laboratory of Sensor Technology and Biomedical Instrument [grant no. 2020B1212060077 (J.W.)], and the Science and Technology Innovation Commission of Shenzhen [grant no. JCYJ20220530145601004 (J.W.)]. **Author contributions:** X.Z. and G.W. performed the experiments, analyzed the data, prepared the figures, and wrote the manuscript. J. Z. and Z.Y. helped to revise and edit the manuscript. J.W. designed the experiments and revised the manuscript. **Competing interests:** The authors declare that they have no competing interests. **Data and materials availability:** All data needed to evaluate the conclusions in the paper are present in the paper and/or the Supplementary Materials.

Submitted 17 January 2023
Accepted 5 February 2024
Published 8 March 2024
10.1126/sciadv.adg7380